JM PAPERS

Mixing of active scalars due to random weak shock waves in two dimensions

Joaquim P. Jossy[1] and Prateek Gupta[1]

[1]Department of Applied Mechanics, Indian Institute of Technology Delhi, New Delhi 110016, India
Corresponding author: Prateek Gupta, prgupta@am.iitd.ac.in

In this work, we investigate the mixing of active scalars in two dimensions by the stirring action of stochastically generated weak shock waves. We use Fourier pseudospectral direct numerical simulations of the interaction of shock waves with two non-reacting species to analyse the mixing dynamics for different Atwood numbers (At). Unlike passive scalars, the presence of density gradients in active scalars alters the molecular diffusion term and makes the species diffusion nonlinear, introducing a concentration gradient-driven term and a density gradient-driven nonlinear dissipation term in the concentration evolution equation. We show that the direction of concentration gradient causes the interface across which molecular diffusion occurs to expand outwards or inwards, even without any stirring action. Shock waves enhance the mixing process by increasing the perimeter of the interface and by sustaining concentration gradients. Negative Atwood number mixtures sustain concentration gradients for a longer time than positive Atwood number mixtures due to the so-called nonlinear dissipation terms. We estimate the time until that when the action of stirring is dominant over molecular mixing. We also highlight the role of baroclinicity in increasing the interface perimeter in the stirring dominant regime. We compare the stirring effect of shock waves on mixing of passive scalars with active scalars and show that the vorticity generated by baroclinicity is responsible for the folding and stretching of the interface in the case of active scalars. We conclude by showing that lighter mixtures with denser inhomogeneities ($At < 0$) take a longer time to homogenise than the denser mixtures with lighter inhomogeneities ($At > 0$).

Key words: turbulent mixing

1. Introduction

Mixing is the process of evolution of constituent concentrations from an initial state of segregation to a final state of homogeneity (Villermaux 2019). Usually, the influence of turbulence on the mixing of passive scalars is studied to quantify turbulent mixing (Sreenivasan 2019). The evolution of the concentration (c) of a passive scalar is governed

by the advection and molecular diffusion terms as shown in (1.1). Molecular diffusion acts across the interface and reduces the mean value of concentration gradients (Eckart 1948). In the absence of advection, mixing by molecular diffusion occurs at a relatively slow rate (Tennekes & Lumley 1972). Any action that affects the advective term of (1.1) is termed as 'stirring'. Stirring enhances the mixing process by increasing the mean value of gradients and increases the area across which molecular diffusion occurs (Eckart 1948). Mixing comprising of both stirring and molecular diffusion can be split into two regimes: the regime where stirring dominates over molecular diffusion and the regime where molecular diffusion becomes the significant contributor to mixing (Meunier & Villermaux 2003; Sreenivasan 2019). In this work, we investigate the stirring effect of nonlinear acoustic waves (weak shock waves) and analyse the mechanism by which shock waves enhance the mixing process.

$$\frac{\partial c}{\partial t} + \boldsymbol{u} \cdot \boldsymbol{\nabla} c = D \nabla^2 c. \tag{1.1}$$

Dimotakis (2005) classifies the mixing process into three levels based on the effect of the mixing constituents on the flow dynamics. The mixing of passive scalars is called level-1 mixing, where the mixing constituents have no effect on the flow dynamics irrespective of the coupling due to density gradients. Examples involve the mixing of pollutants, dyes, smoke particles, etc. in fluid. The mixing of active scalars is termed as level-2 mixing, where the mixing process is coupled with the flow dynamics through density gradients. Rayleigh–Taylor and Ritchymer–Meshkov instabilities (RMI) (Richtmyer 1954; Meshkov 1969) are examples of level-2 mixing. Mixing that proceeds with changes in fluid composition is called level-3 mixing. Combustion and detonations are some of the best examples of level-3 mixing. There exists an abundant literature on the mixing of passive scalars in both incompressible and compressible flow fields. Experimental studies on the mixing of passive scalars show that scalar gradients decay with time, and the role of vorticity in turbulent fields is to sustain scalar gradients (Buch & Dahm 1996). Meunier & Villermaux (2003) study the mixing of a passive scalar blob using a diffusing Lamb–Oseen type vortex, and show that the changes in concentration can be used to indicate the time in which the effect of stirring is dominant. They identify 'mixing time' as an indicator to denote the time during which the action of stirring is dominant over molecular diffusion. They show that the maximum concentration grows linearly until a mixing time is reached, after which it decays in time as $t^{-3/2}$. Schumacher & Sreenivasan (2005) derive a relation between the geometrical properties and the mixing statistics of passive scalars using direct numerical simulations (DNS) of a stochastically forced isotropic turbulent field. They relate the area-to-volume ratio to the passive scalar concentration fluctuations and show that the fluctuations mostly follow a Gaussian distribution. Ni (2016) reports that the convolution of scalar fields in forced compressible turbulent flow fields is more pronounced in forcing schemes with a higher ratio of solenoidal-to-dilational components. In a similar study, John *et al.* (2019) show that the breakdown of the passive scalar field depends on the solenoidal components and that the role of compressibility is negligible in the mixing of passive scalars. Gao *et al.* (2020) challenge the idea of negligible compressibility effects on mixing by showing the alignment of shock with scalar gradients affects mixing in a canonical shock–turbulence interaction configuration. However, only a few studies exist that analyse the level-2 and level-3 mixing in compressible flows. In this work, we analyse the level-2 mixing of two non-reacting fluids of different densities and study the effect of density inhomogeneity on mixing and flow dynamics in a randomly forced shock-wave field in a two-dimensional set-up.

Ritchymer–Meshkov instabilities refer to the growth of perturbations in the interface between two fluids of different densities under the influence of an impulsive acceleration. Ritchymer–Meshkov instabilities are observed in various man-made applications such as inertial-confinement fusion and supersonic combustion (Thomas & Kares 2012; Yang *et al.* 1993; Zhou *et al.* 2021), as well as naturally occurring phenomena in astrophysics (Burrows 2000; Arnett 2000; Zhou 2017). In cases where shock waves are used for impulsively accelerating the interface, the baroclinic vorticity generated at the interface by the misalignment of pressure gradients and density gradients triggers the growth of perturbations on the interface. The growth of these perturbations triggers other instabilities like Kelvin–Helmholtz instabilities (KHIs), leading to enhanced mixing (Brouillette 2002; Zhou 2024). The RMI enhanced mixing plays an important role in the design of inertial-confinement fusion reactors (Thomas & Kares 2012; Zhou *et al.* 2025), and the combustion chambers of supersonic air-breathing engines (Yang *et al.* 1993). The change in interface profile caused by RMI is used to develop stellar evolution models to explain the evolution of supernovae explosions (Burrows 2000; Arnett 2000). Ritchymer–Meshkov instabilities are also the fundamental process for studying shock–flame interactions, where the density difference between the two species is used to model burnt and unburnt fuel mixtures, and the passage of shock waves is used to study the flame propagation and the formation of detonation waves (Al-Thehabey 2020). Primarily, the interfacial mixing and the dynamics of the interface are studied in RMI. Yu *et al.* (2021) show that density gradients across the interface govern the mixing rate. They derive an exact mixing rate expression and show the difference in mixing rates during different stages of RMI. Gao *et al.* (2016) use Favre averaging of mass fraction to derive the growth rate of the mixing zone width and show that compressibility suppresses the mixing rate for a single pass RMI case. They also report a reduction in the role of the diffusion term in mixing with time. The interface dynamics in RMI are explained in terms of the kinematics of the large-scale coherent structures: spikes (penetration of denser fluid into lighter fluid) and bubbles (penetration of lighter fluid into denser fluid). Zhang (1998) uses the Layzer-type model (infinite density ratio across the interface) to show that spikes and bubbles have different growth rates. Herrmann *et al.* (2008) report that bubbles across interfaces of similar density differences move faster and flatten slower compared with interfaces of higher density differences. They conclude that the evolution of the interface is a non-local and multiscale process. Li *et al.* (2021) develop an analytical model to explain the compression and stretching effect of the mixing layer for a single passage of shock wave. They also show that the mixing triggered by RMI lasts even after the passage of the shockwave. In the present work, we use stochastically forced shock waves to induce multimodal perturbations on the interface. We study the mixing induced by such shock waves across interfaces of different density ratios. To this end, we use a simplified two-dimensional model to analyse the mixing characteristics and interface dynamics resulting from continuous and stochastic forcing of a set-up resembling that of RMI using shock-resolved DNS of the fully compressible Navier–Stokes equations.

In this work, we analyse the mixing of active scalars driven by random shock waves. We consider binary mixtures of two non-reacting species with different density ratios. Throughout, we consider a circular shaped inhomogeneity (blob) with a smaller area than the rest of the domain. In § 2, we discuss the governing equations we use to study the mixing enhancement effect of shock waves. We also discuss the details of the numerical set-up and the parameters used to carry out the shock-resolved DNS. In § 3, we first discuss the effect of density gradients on the diffusion of active scalar without shock waves. We use a simplified one-dimensional (1-D) nonlinear diffusion equation to show that the direction of the density gradients affects the evolution of mass fraction due to nonlinear

diffusion. We next show the stirring effect of shock waves and its role in enhancing the mixing. We also show the role of baroclinicity in increasing the perimeter across which diffusion occurs before concluding with a summary of our findings in § 4.

2. Governing equations and numerical simulations

In this section, we discuss the governing equations and the numerical method used to study the mixing of two non-reacting species by stochastically forced shock waves. We use the previously developed forcing scheme for generating a random shock-wave field (Jossy & Gupta 2023) and summarise it below along with the parameter space.

We use the dimensionless form of the Navier–Stokes and species equation to analyse the mixing of active scalars by shock waves. A non-reacting binary mixture is used to create different density inhomogeneities by varying the molecular weight (W_i) of the species. The dimensionless equations of the density ρ, velocity $\boldsymbol{u}$, pressure p and concentration of the ith species Y_i (mass fraction) are given by

$$\frac{\partial \rho}{\partial t} + \boldsymbol{\nabla} \cdot (\rho \boldsymbol{u}) = 0, \tag{2.1}$$

$$\frac{\partial \boldsymbol{u}}{\partial t} + \boldsymbol{u} \cdot \boldsymbol{\nabla} \boldsymbol{u} + \frac{\boldsymbol{\nabla} p}{\rho} = \frac{1}{\rho Re_{ac}} \left(\boldsymbol{\nabla} \cdot (2\mu \boldsymbol{S}) \right) + \frac{1}{\rho Re_{ac}} \left(\boldsymbol{\nabla} \cdot \left(\kappa - \frac{2\mu}{3} \right) \boldsymbol{D} \right) + \boldsymbol{F}, \tag{2.2}$$

$$\frac{\partial p}{\partial t} + \boldsymbol{u} \cdot \boldsymbol{\nabla} p + \gamma p \boldsymbol{\nabla} \cdot \boldsymbol{u} = \frac{1}{Re_{ac} Pr} \boldsymbol{\nabla} \cdot (\alpha \boldsymbol{\nabla} T) + \frac{\gamma - 1}{Re_{ac}} \left(2\mu \boldsymbol{S} : \boldsymbol{S} + \left(\kappa - \frac{2\mu}{3} \right) \boldsymbol{D} : \boldsymbol{D} \right), \tag{2.3}$$

$$\frac{\partial Y_i}{\partial t} + \boldsymbol{u} \cdot \boldsymbol{\nabla} Y_i = \frac{1}{\rho \, Re_{ac} Sc} \boldsymbol{\nabla} \cdot \left(\rho \frac{W_i}{W} \boldsymbol{\nabla} X_i \right), \tag{2.4}$$

where W is the mean molecular mass of the mixture, and X_i is the mole fraction of the ith species related to the mass fraction Y_i as

$$X_i = \frac{W}{W_i} Y_i. \tag{2.5}$$

We combine the above equations using the dimensionless equation of state for an ideal gas mixture,

$$\gamma p = \frac{\rho}{W} T, \tag{2.6}$$

where

$$\frac{1}{W} = \frac{Y_1}{W_1} + \frac{Y_2}{W_2}. \tag{2.7}$$

We use the pressure equation (2.3) derived from the conservative energy equation and the internal energy equation for an ideal gas (Kundu *et al.* 2015). We note that solving pressure equation is equivalent to solving the internal energy equation for a perfect gas. Moreover, the pressure equation has been extensively used previously in mixing and compressible turbulence studies spanning all ranges of Mach numbers (Sarkar *et al.* 1991; Sarkar 1995; Pantano *et al.* 2003). In (2.2) and (2.3), $\boldsymbol{S}$ and $\boldsymbol{D}$ are the strain rate and dilatation tensors, respectively, given by

$$\boldsymbol{S} = \frac{1}{2} \left(\boldsymbol{\nabla} \boldsymbol{u} + \boldsymbol{\nabla} \boldsymbol{u}^T \right), \ \boldsymbol{D} = (\boldsymbol{\nabla} \cdot \boldsymbol{u}) \, \boldsymbol{I}. \tag{2.8}$$

The fluid properties such as dynamic viscosity (μ), bulk viscosity (κ) and thermal conductivity (α) are all dimensionless. The flow properties are governed by the dimensionless numbers, the acoustic Reynolds number (Re_{ac}), the Prandlt number (Pr) and the Schmidt number (Sc) defined as

$$Re_{ac} = \frac{\rho_m c_m L_m}{\mu_m}, \quad Pr = \frac{\gamma \mu_m \tilde{R}}{(\gamma - 1) W_m \alpha_m}, \quad Sc = \frac{\mu_m}{\rho_m \lambda_m}. \tag{2.9}$$

The flow field parameters are scaled using the characteristic dimensional quantities which are denoted by the subscript $()_m$. The velocity is scaled using the characteristic speed of sound c_m, and $\tilde{R}$, μ_m, α_m and λ_m denote the universal gas constant, dimensional viscosity, thermal conductivity and diffusion coefficient, respectively. Since we use dimensionless equations in our numerical simulations, the specific values of the characteristic scales hold no significance. We also assume that the heat capacities of both the species are the same.

We refer the reader to our earlier work (Jossy & Gupta 2023) for a detailed derivation of the dimensionless governing equations (2.1)–(2.3) and the appropriate characteristic scales of the quantities. The forcing term $\boldsymbol{F}$ in (2.2) is used to generate shock waves. For species diffusion, we use the Hirschfelder and Curtiss approximation (Hirschfelder *et al.* 1964; Poinsot & Veynante 2005) in (2.4) with a constant equivalent diffusion coefficient. As we discuss in later sections, the nonlinear diffusive flux in (2.4) results in a translation of the active scalar interface, resulting in an expansion or contraction of the inhomogeneities, depending on the value of the molecular mass ratio.

2.1. *Fourier pseudospectral simulations*

We perform shock-resolved DNS of the fully compressible two-dimensional Navier–Stokes equations (2.1)–(2.3) and the species equation (2.4) using an MPI (message passing interface) parallelised Fourier pseudospectral solver (Boyd 2001). We note that both the momentum (2.2) and the pressure equation (2.3) are used in the non-conservative form in this work. Since the derivatives are calculated using the exact relation $\widehat{\nabla \phi} = i \mathbf{k} \hat{\phi}$ (where $\hat{\phi}$ denotes the Fourier transform of a field ϕ), the non-conservative form of the equations poses no limitations. We use the Runge–Kutta fourth-order scheme for time stepping and ensure numerical stability using the 2/3 dealiasing method in the nonlinear terms only to eliminate the aliasing errors. As we show later, nonlinearities are negligible for length scales much larger than the length scale below which the aliasing errors are removed. For all the simulations discussed in the work, we consider 3072 Fourier modes in each direction such that the nonlinear terms are resolved until $k_{max} = 1024$. We show in §2.2 and the convergence study in appendix A that the resolution is sufficient to resolve all the scales for the values of the energy injection rate (ε in (2.13)) used in this work. Each simulation is run using 256 cores consuming approximately 10^5 core hours. We consider constant viscosity ($\mu = 1$) and thermal conductivity ($\alpha = 1$) for all our simulations and ignore bulk viscosity ($\kappa = 0$) for simplicity. For all simulations, we consider $Pr = Sc = 0.7$, such that the molecular diffusion and heat diffusivity remain the same. We initialise our simulations using quiescent ($\boldsymbol{u} = 0$), isobaric (uniform pressure) and isothermal (uniform temperature) conditions with a circular blob of radius $\pi/2$. We specify the species having a circular distribution using the tanh function to specify the initial concentration field, as follows:

$$Y_c = \frac{1}{2} \left[1 - \tanh \left(\frac{1}{\delta} \left(\sqrt{(x - \pi)^2 + (y - \pi)^2} - \frac{\pi}{2} \right) \right) \right]. \tag{2.10}$$

The species constituting the blob has density ρ_c and the surrounding species has density ρ_s. We use subscript $()_c$ to indicate the species inside the circular blob and the subscript $()_s$ to denote the surrounding species. We use the parameter value $\delta = 1/15$ in (2.10) to obtain a steep but smooth concentration distribution to achieve a diffused thin interface. The parameter δ represents a characteristic interface thickness and will be used later to calculate the apparent perimeter of the interface during mixing.

The forcing $\boldsymbol{F}$ in (2.2) is similar to the one used by Jossy & Gupta (2023). For completeness, we provide a brief overview here. The forcing $\boldsymbol{F}$ is defined in the Fourier space and computed using four statistically independent Uhlenbeck–Ornstein (UO) (Eswaran & Pope 1988) processes ($a_{i,\boldsymbol{k}}(t)$ for $i = 1, 2, 3$ and 4), satisfying the following conditions:

$$\langle a_{i,\boldsymbol{k}}(t)\rangle = 0, \tag{2.11}$$

$$\langle a_{i,\boldsymbol{k}}(t)a^*_{j,\boldsymbol{k}}(t+s)\rangle = 2\sigma^2 \boldsymbol{\delta}_{ij} \exp(-s/T_L), \tag{2.12}$$

where $\langle \cdot \rangle$ denotes the ensemble average, $()^*$ denotes the complex conjugate, σ^2 is the variance, and T_L is the forcing timescale. To prevent any direct effect of energy injection at small length scales, we restrict our forcing to larger scales within the band of wavenumbers $0 < |\boldsymbol{k}| < k_F$, where $k_F = 5$ in all our simulations. The total rate of energy injection ε is a function of the variance σ^2, the time scale T_L of the UO process, and the number of wave vectors within the forcing band N_F and is given by

$$\varepsilon = 4N_F T_L \sigma^2. \tag{2.13}$$

The forcing vector in the Fourier space can be obtained by combining the four independent processes as

$$\widehat{\boldsymbol{a}}_{\boldsymbol{k}} = \left(a_{1,\boldsymbol{k}} + i a_{2,\boldsymbol{k}}, a_{3,\boldsymbol{k}} + i a_{4,\boldsymbol{k}}\right)^T. \tag{2.14}$$

To force only the acoustical component of velocity, we remove the vortical component from $\widehat{\boldsymbol{a}}_{\boldsymbol{k}}$ yielding

$$\widehat{\boldsymbol{F}}_{\boldsymbol{k}}(t) = \frac{(\widehat{\boldsymbol{a}}_{\boldsymbol{k}}(t) \cdot \boldsymbol{k})}{|\boldsymbol{k}|^2}\boldsymbol{k}. \tag{2.15}$$

It has been shown that decaying acoustic wave turbulence has similar behaviour to Burgers turbulence (Gupta & Scalo 2018). We speculate that the behaviour of stochastically forced shock waves may be similar to that of two-dimensional forced Burgers turbulence (Cho *et al.* 2014). A detailed comparison between the two is beyond the scope of the current study. In our earlier work (Jossy & Gupta 2023), we have used the stochastic forcing method described above to generate a field of isotropic shock waves. The wave energy spectra of the random shock waves generated exhibit identical dependence on the dissipation and the integral length scale as decaying 1-D turbulence (Gupta & Scalo 2018) as well as shallow water wave-turbulence (Augier *et al.* 2019). Augier *et al.* (2019) derive the shallow water wave-turbulence scaling laws assuming isotropy, independent of the dispersive nature of the shallow water waves. Hence, the forcing method mentioned in (2.15) generates a field of isotropic random shock waves whose phasing changes at every time instant in a homogeneous mixture. Reflections of the shock waves at the inhomogeneity interface may introduce some spatial anistropy, a detailed analysis of which is deferred to future studies and is beyond the scope of the current work. As mentioned earlier, in this work, we study the interaction of forced weak shock waves, which induce multimodal perturbations on the inhomogeneity interface separating the two species and thus influencing the active scalar mixing dynamics.

S. No	Active/passive	At	χ	Indicator
1	Passive	–	–	PS*
2	Active	0.5	3	$At = 0.5$*
3	Active	-0.5	0.33	$At = -0.5$*

Table 1. Parameter space for simulations considering only the effect of molecular diffusion without any shock waves along with their indicators.

2.2. Simulation parameters

To study the effect of forced weak shock waves on the mixing of species with different densities, we use the Atwood number (At), defined as

$$At = \frac{\rho_s - \rho_c}{\rho_s + \rho_c} = \frac{\chi - 1}{\chi + 1}. \tag{2.16}$$

We study the effect of shock waves in both a denser mixture ($\chi > 1$) and a lighter mixture ($\chi < 1$), where χ is the density ratio of surrounding species to the blob species. To understand the effect of density gradients on the species diffusion alone, we run one case each of positive and negative Atwood numbers without any shocks and compare them with a passive scalar case. Table 1 shows the parameters of the simulation cases without any shock waves. We study the effect of weak shock waves on mixing for three values of positive and negative Atwood numbers each and compare their mixing dynamics with a passive scalar case. Since each realisation of the stochastic forcing $\boldsymbol{F}$ is different, the mixing process itself is a stochastic non-equilibrium process. Hence, we simulate additional realisations of the end ranges of the Atwood number, i.e. four realisations of $At = \pm 0.75$ and three realisations of $At = \pm 0.25$ to show that the mixing characteristics are consistent across Atwood numbers for different realisations of the same forcing parameters. The average of the different realisations is represented by the superscript $()^{\dagger}$.

As mentioned earlier, we choose $k_{max} = 1024$ to discuss the results of the study. But to show that the chosen resolution is sufficient, we run additional simulations with $k_{max} = 768$ and $k_{max} = 1536$, which are denoted by the superscripts $()^{\star}$ and $()^{\ddagger}$, respectively. The details of the convergence study are given in appendix A. Table 2 shows the simulation cases used to study the stirring effect of shock waves. For all simulations, we inject acoustic energy at the rate of $\varepsilon/4N_F = 1.25 \times 10^{-6}$ to generate weak shock waves ($\langle M \rangle < 1.1$). We run all the realisations for all the cases for sufficiently long times until the effects of molecular diffusion take over the effects of stirring. We run one realisation for all the different Atwood numbers shown in table 2 further close to homogenisation. The smallest length scales generated in the simulations correspond to the shock thickness scale η (Donzis 2012; Larsson *et al.* 2013; Gupta & Scalo 2018; Jossy & Gupta 2023) and the Batchelor scale η_B, which are related to the acoustic Reynolds number Re_{ac} as

$$\eta \sim \frac{1}{Re_{ac}}(\varepsilon \ell)^{-1/3}, \quad \eta_B = \frac{\eta}{\sqrt{Sc}}, \tag{2.17}$$

S. No	Active/passive	At	χ	$\langle M \rangle$	$\langle \eta \rangle_t$	$\langle \eta_B \rangle_t / \Delta$	k_{max}	Indicator
1	Passive	–	–	1.09	0.032	12.2	768	PS*
2	Passive	–	–	1.09	0.031	12.2	1024	PS
3	Passive	–	–	1.09	0.031	12.2	1536	PS‡
4	Active	0.25	1.67	1.08	0.039	15.8	768	$At = 0.25^\star$
5	Active	0.25	1.67	1.08	0.038	15.8	1024	$At = 0.25^\dagger$
6	Active	0.25	1.67	1.08	0.038	15.8	1536	$At = 0.25^\ddagger$
7	Active	0.5	3.0	1.07	0.023	9.3	768	$At = 0.5^\star$
8	Active	0.5	3.0	1.07	0.023	9.3	1024	$At = 0.5$
9	Active	0.5	3.0	1.07	0.023	9.3	1536	$At = 0.5^\ddagger$
10	Active	0.75	7.0	1.07	0.019	7.7	1024	$At = 0.75^\dagger$
11	Active	0.75	7.0	1.07	0.019	7.7	1536	$At = 0.75^\ddagger$
12	Active	−0.25	0.6	1.08	0.029	11.8	1024	$At = -0.25^\dagger$
13	Active	−0.5	0.33	1.07	0.028	11.3	1024	$At = -0.5$
14	Active	−0.75	0.1428	1.08	0.022	9.37	1024	$At = -0.75^\dagger$

Table 2. Parameter space for simulations with stochastically generated shock waves and their corresponding indicators. In the above table, $\langle M \rangle$ represents the area averaged Mach number of the shock waves in the domain, $\langle \eta \rangle_t$ represents the time-averaged shock thickness scale and $\langle \eta_B \rangle$ represents the time averaged Batchelor scale.

where $\ell = 2/k_F$ is the integral length scale, which represents the mean distance between two shocks. To ensure shock-resolved simulations, we consider $Re_{ac} = 1000$, such that $k_{max}\eta > 1.5$ and follow an even more strict resolution scale for mixing, $\eta_B/\Delta > 0.5$ (Schumacher *et al.* 2005) where Δ is given by $2\sqrt{2}\pi/3k_{max}$. To show resolution in all our simulations, we calculate the binned density-weighted wave spectral energy $\widehat{E}_{wk}$ and the spectral flux of the wave energy $\widehat{\Pi}_{wk}$ whose definitions are given in (2.18) and (2.19), respectively. We direct the reader to previous studies (Miura & Kida 1995; Jossy & Gupta 2023) for the detailed derivation of the density-weighted spectral quantities. We use a density-weighted velocity $\boldsymbol{w} = \sqrt{\rho}\boldsymbol{u}$ and its wave component obtained upon the Helmholtz decomposition (Miura & Kida 1995; Jossy & Gupta 2023). Denoting the Fourier transform of a quantity ϕ by $\hat{\phi}$ and the complex conjugate by $\hat{\phi}^*$, the density-weighted wave spectral energy $\widehat{E}_{wk}$ and its transfer function $\widehat{\mathcal{T}}_{wk}$ are obtained as

$$\widehat{E}_{wk} = \frac{1}{2}\left(\widehat{\boldsymbol{w}}_{wk}^* \cdot \widehat{\boldsymbol{w}}_{wk} + \widehat{\left(p - \frac{1}{\gamma}\right)}_k^* \widehat{\left(p - \frac{1}{\gamma}\right)}_k\right), \qquad (2.18)$$

$$\widehat{\mathcal{T}}_{wk} = \mathcal{R}\left[\widehat{\boldsymbol{w}}_{wk}^* \cdot \widehat{\left(\frac{\nabla p}{\sqrt{\rho}}\right)}_k + \widehat{\left(p - \frac{1}{\gamma}\right)}_k^* \widehat{\nabla \cdot \boldsymbol{u}}_{wk}\right]$$

$$+ \mathcal{R}\left[\hat{\boldsymbol{w}}_{wk}^* \cdot \widehat{\left(\boldsymbol{w} \cdot \nabla \boldsymbol{u}\right)}_{wk} - \widehat{\boldsymbol{w}}_{wk}^* \cdot \widehat{\left(\frac{\left(p - \frac{1}{\gamma}\right)\nabla p}{\sqrt{\rho}}\right)}_k\right]$$

$$+ \mathcal{R}\left[\gamma \widehat{\left(p - \frac{1}{\gamma}\right)}_k^* \widehat{\left(\left(p - \frac{1}{\gamma}\right)\nabla \cdot \boldsymbol{u}\right)}_{wk} + \widehat{\left(p - \frac{1}{\gamma}\right)}_k^* \widehat{\left(\boldsymbol{u} \cdot \nabla p\right)}_{wk}\right], \qquad (2.19)$$

where the subscript $()_{wk}$ denotes the Fourier transform of the wavefield, and $\mathcal{R}()$ denotes the real part of the quantity. Equations (2.18) and (2.19) are derived using the second-order approximation of (2.1)–(2.3) (see Jossy & Gupta (2023) for a detailed derivation). The
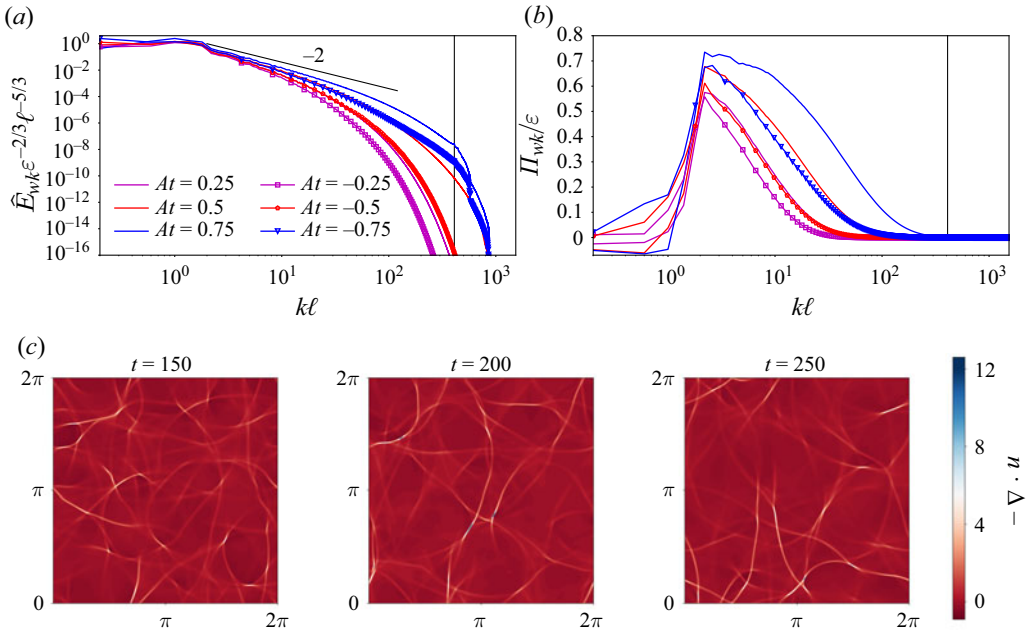
1007 A25-8

Figure 1. Dimensionless scaled density-weighted wave energy $\hat{E}_{wk}$ spectra (*a*) and spectral flux of wave energy $\widehat{\Pi}_{wk}$ (*b*) of active scalars cases in table 2 averaged over the time interval $t = 50$ to $t = 300$. The vertical lines in both the figures show the dealiasing limit $k_{max}\ell$. The spectral flux is negligible beyond the $k_{max}\ell$ limit highlighting that all the nonlinear scales are resolved. The legends are identical for both the figures. Contours of divergence at different time instances for $At = 0.5$ (*c*).

term $p - \frac{1}{\gamma}$ is the change in pressure from the isobaric base state at the dimensionless pressure of $1/\gamma$. Figure 1(*a*) shows the scaled density-weighted wave energy spectra $\widehat{E}_{wk}\varepsilon^{-2/3}\ell^{-5/3}$ versus the scaled wavenumber $k\ell$. Since the forcing acts only within $0 < k\ell < 2$, wave energy in the further wavenumbers highlights forward spectral wave energy cascade due to the nonlinear terms in the governing equations. Since the generated shock waves are weak, $\widehat{E}_{wk}$ decays as k^{-2} before decaying rapidly due to thermoviscous dissipation. Figure 1(*b*) shows the scaled flux of the spectral wave energy $\widehat{\Pi}_{wk}/\varepsilon$ calculated as the cumulative sum of the transfer function $\widehat{\mathcal{T}}_{wk}$ in (2.19). The spectral flux approaches net dissipation (equal to net energy injection) and then decays after a decade as the wavenumber increases. Unlike hydrodynamic turbulence, thermoviscous dissipation is significant at all scales in a field of random shock waves since the wave energy $\sim k^{-2}$ and the dissipation scales as $k^2 \widehat{E}_{wk}$ approximately. Similar values of spectral flux and the net energy injection highlight that the waves generated are nonlinear. Decay of the spectral flux in figure 1 before $k_{max}\ell$ for all the cases shows that nonlinearities become negligible for length scales approaching $1/k_{max}$. Since the dealiasing is used only in the nonlinear terms, any linear dynamics at length scales smaller than $1/k_{max}$ until $1/3072$ are well resolved. In appendix A, we show that the wave energy spectra for $k > k_{max}$ are modified slightly only for $At = 0.75$ case for $k_{max} = 1536$. However, the energy in these scales is more than seven orders of magnitude smaller than the integral length scale energy. Hence, these scales have negligible influence on the mixing dynamics, which are governed by the pressure variations leading to baroclinicity (see §§ 3.2 and 3.3). Yet, we show the contours and discuss the effects of weak shock waves on mixing dynamics using $At = \pm 0.5$ cases, for which all the scales are resolved for $k_{max} = 1024$ as shown in appendix A.

The variation of density-weighted wave spectra across different Atwood number cases occurs due to the variation in density across the inhomogeneity interface. Stretching and folding of the inhomogeneity generate smaller scales in the interface. However, the scale corresponding to the interface thickness increases due to molecular diffusion. As discussed later in § 3.1, the molecular diffusion term responsible for the diffusion of the interface (later termed as the Laplacian diffusion term) and the molecular diffusion term responsible for the movement of the interface due to the density gradients (later termed as the nonlinear dissipation term) change with the Atwood number (cf. (3.4)). For $At > 0$, the Laplacian diffusion term dominates the nonlinear dissipation term. As $At > 0$ increases, the Laplacian diffusion coefficient decreases, indicating relatively smaller scales maintained for higher values of $At > 0$ in figure 1(*a*). As $At < 0$ decreases, the nonlinear dissipation coefficient increases resulting in more rapid expansion of the interface. This results in more collisions of the shock waves with the interface generating smaller scales in the interface for more negative At cases. For the same value of $|At|$, the $At > 0$ mixture seems to exhibit more energy in smaller length scales compared with the $At < 0$ mixture, as evident from figure 1(*a*). Hence, in the convergence study discussed in appendix A, we run $At > 0$ cases at higher resolution. It is important to note that in figure 1, the density gradients due to mixture being inhomogeneous have the smallest contribution for $At = \pm 0.25$ cases since the density values of the two species are the closest among the cases considered.

In viscous compressible simulations, shocks can be identified by the negative divergence lines (Samtaney *et al.* 2001; Augier *et al.* 2019). Figure 1(*c*) shows the contours of negative divergence for $At = 0.5$ at different time instances. The high negative values of divergence are indicative of the presence of shocks in the field. To quantify the strength of the random shock waves generated, we calculate the shock Mach number using the dimensionless entropy. The entropy for a mixture of species is defined as (Liepmann & Roshko 2001)

$$s = \frac{1}{W}\left(\frac{\gamma}{\gamma-1}\log\frac{T}{T_o}\right) - \sum_{i=1}^{2}\frac{1}{W_i}\log\frac{p_i}{p_{io}}, \qquad (2.20)$$

where p_i is the partial pressure of species i and the subscript $()_o$ indicates the initial state of the species. At a point in the domain, entropy changes due to mixing as well as the entropy generated due to shocks. To isolate the entropy generated due to the shock waves only, we calculate the entropy jump only in the regions where the divergence is negative ($\nabla \cdot \boldsymbol{u} < 0$). We calculate the approximate entropy jump using the entropy field s as

$$\Delta s \approx \left|\frac{\partial s}{\partial x}\right| dx + \left|\frac{\partial s}{\partial y}\right| dy. \qquad (2.21)$$

Using the entropy jump field Δs, we calculate the Mach number field assuming weak shocks using

$$M = \sqrt{1 + \left(\frac{3\Delta s(\gamma+1)^2}{2\gamma}\right)^{1/3}}. \qquad (2.22)$$

Figure 2(*a*) shows the contours of Mach number for the case $At = 0.5$ at $t = 250$. We note that the points at which the Mach number peaks correlate with those at which $-\nabla \cdot \mathbf{u}$ peaks in figure 1(*c*). In figure 2(*b*), we show the time-averaged normalised histogram or probability distribution function (PDF) of the Mach number field M for all the Atwood number cases with shocks. Since the shock waves are very thin, most of the domain
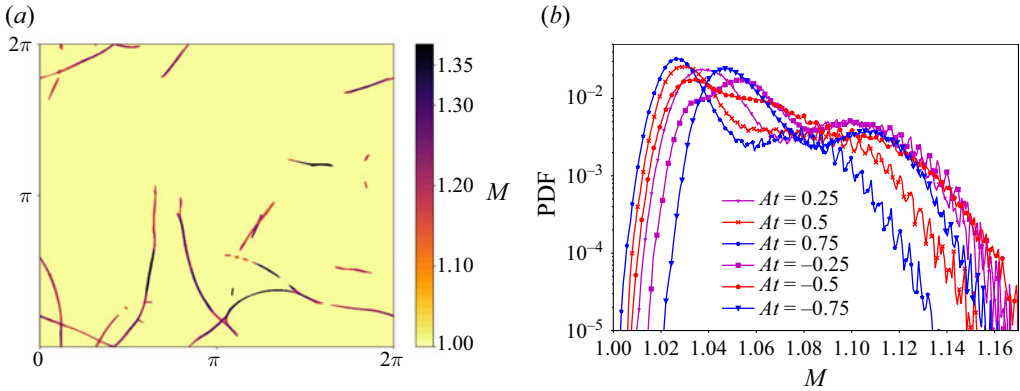
(*a*)

(*b*)

Figure 2. Mach number contours of $At = 0.5$ at $t = 250$ calculated using (2.22) (*a*) Time averaged normalised histogram of the Mach number of active scalars cases in table 2 (*b*).

exhibits Mach number very close to 1. A single value of the representative mean Mach number for all the cases with shocks is shown in table 2.

3. Results and discussion

In this section, we present the mixing effects of the forced shock waves on active scalars in a two-dimensional set-up. Density gradients affect both the advection and diffusion of active scalars. In the presence of shock waves, the baroclinic interaction of density gradients with shock waves results in a vorticity field, which tends to deform the blob and increase the total apparent interface perimeter through advection. Additionally, the density-weighted nonlinear diffusion of active scalars is significantly different from the diffusion of passive scalars. We first discuss the mixing of active scalars in the absence of shock waves to isolate the effect of the density gradients on the diffusion process. We then discuss the enhancement of mixing by shock waves and finally discuss the role of baroclinicity in increasing the apparent perimeter of the interface through advection. We present the contours of $At = \pm 0.5$ cases for visualisation wherever necessary and use $At = \pm 0.25$ and $At = \pm 0.75$ cases to discuss the effects of Atwood number on the mixing dynamics.

3.1. *Effect of density gradients on nonlinear molecular diffusion*

The role of molecular diffusion in passive scalars is to reduce the mean value of concentration gradients. In this section, we analyse the effect of density gradients on the nonlinear molecular diffusion process of active scalars. To isolate the effect of density gradients on mixing by molecular diffusion, we consider cases $At = 0.5^*$ and $At = -0.5^*$ where mixing is solely due to molecular diffusion. These cases are compared with the diffusion of a passive scalar case PS^* in table 1, where no density gradients are present. In these three cases, $\boldsymbol{F}$ in (2.2) is set to zero. Without shock waves, the advective term of the concentration evolution equation becomes negligible, and (2.4) can be approximated as

$$\frac{\partial Y_i}{\partial t} = \frac{1}{\rho Re_{ac} Sc} \nabla \cdot \left(\rho \frac{W_i}{W} \nabla X_i \right). \tag{3.1}$$

The right-hand side of (3.1) can be written as follows:

$$\frac{1}{\rho \, Re_{ac} \, Sc} \nabla \cdot \left(\rho \frac{W_i}{W} \nabla X_i \right) = \frac{1}{\rho \, Re_{ac} \, Sc} \nabla \cdot \left(\rho \frac{\nabla W}{W} Y_i + \rho \nabla Y_i \right). \quad (3.2)$$

The right-hand side of (3.2) represents the diffusion of an active scalar. Unlike the linear diffusion of a passive scalar (cf. (1.1)), which depends only on the concentration gradients, the diffusion of an active scalar also depends on the mean molecular mass gradients and is nonlinear. Using the definition of mean molecular mass and the mass fraction conservation constraint ($Y_c + Y_s = 1$), the equation for the evolution of the circular species (Y_c) can be written in terms of gradients of species concentration as

$$\frac{\partial Y_c}{\partial t} = \frac{1}{Re_{ac} \, Sc} \left(\underbrace{D_1 \nabla^2 Y_c}_{I} + \underbrace{D_2 \nabla Y_c \cdot \nabla Y_c}_{II} + \underbrace{\frac{D_1}{\rho} (\nabla \rho \cdot \nabla Y_c)}_{III} \right), \quad (3.3)$$

where D_1 and D_2 are defined as

$$D_1 = \frac{1}{1 + (\chi - 1)Y_c}, \quad D_2 = \frac{1 - \chi}{(1 + (\chi - 1)Y_c)^2}. \quad (3.4)$$

The second and third terms in (3.3) are additional terms modifying the diffusion of active scalars. The effect of these terms is shown in the contours of Y_c at different time instances in figures 3(*a*) and 3(*b*), for $At > 0$ and $At < 0$, respectively. We see that for the $At > 0$ (denser mixture, lighter blob), the interface moves inwards, and the blob seems to shrink, while for $At < 0$ (lighter mixture, denser blob), the interface moves outwards, and the blob seemingly expands. This highlights the biased diffusion process in active scalars, where the interface moves towards the lighter species. The two terms mentioned above (II and III in (3.3)) are similar to the scalar dissipation term analysed in the mixing of shock–bubble interaction studies and hence, are referred to as nonlinear dissipation terms (Tomkins *et al.* 2008; Yu *et al.* 2021). Specifically, we choose to call II and III in (3.3) the concentration-gradient-driven and density-gradient-driven dissipation, respectively, in the current study. Figure 6(*a*) shows the evolution of radius R at which the maximum value of $|\nabla Y_c|$ is located from the centre of the blob. We see that for the lighter blob case ($At = 0.5$), the interface moves inwards, while for the heavier blob case ($At = -0.5$), the interface moves outwards. We also see that in the passive scalar diffusion, there is very little movement of the interface. To illustrate that the nonlinear dissipation terms (II and III in (3.3)) are indeed responsible for the movement of the interface, we solve a 1-D unsteady nonlinear conduction equation,

$$\frac{\partial Y}{\partial t} = D \frac{\partial^2 Y}{\partial x^2} + K \left(\frac{\partial Y}{\partial x} \right)^2, \quad (3.5)$$

with $K = \pm 1$ for the same initial condition as (2.10) and $D = 1/10$ in one dimension.

Figure 6(*b*) shows the evolution of Y governed by (3.5) with $K = \pm 1$. We see that for positive coefficients, the interface moves outwards, while for negative coefficients, the interface moves inwards. Hence, the essential physics of the movement of the interface is captured by the nonlinear conduction equation (3.5) highlighting that the nonlinear diffusion terms in (3.3) result in the movement of the interface, while the Laplacian term diffuses the interface as usual. These observations agree with the known diffusive travelling wave type solutions of nonlinear conduction equations (Atkinson *et al.* 1981). Additionally, these results are also in line with the observations in figure 6(*a*),
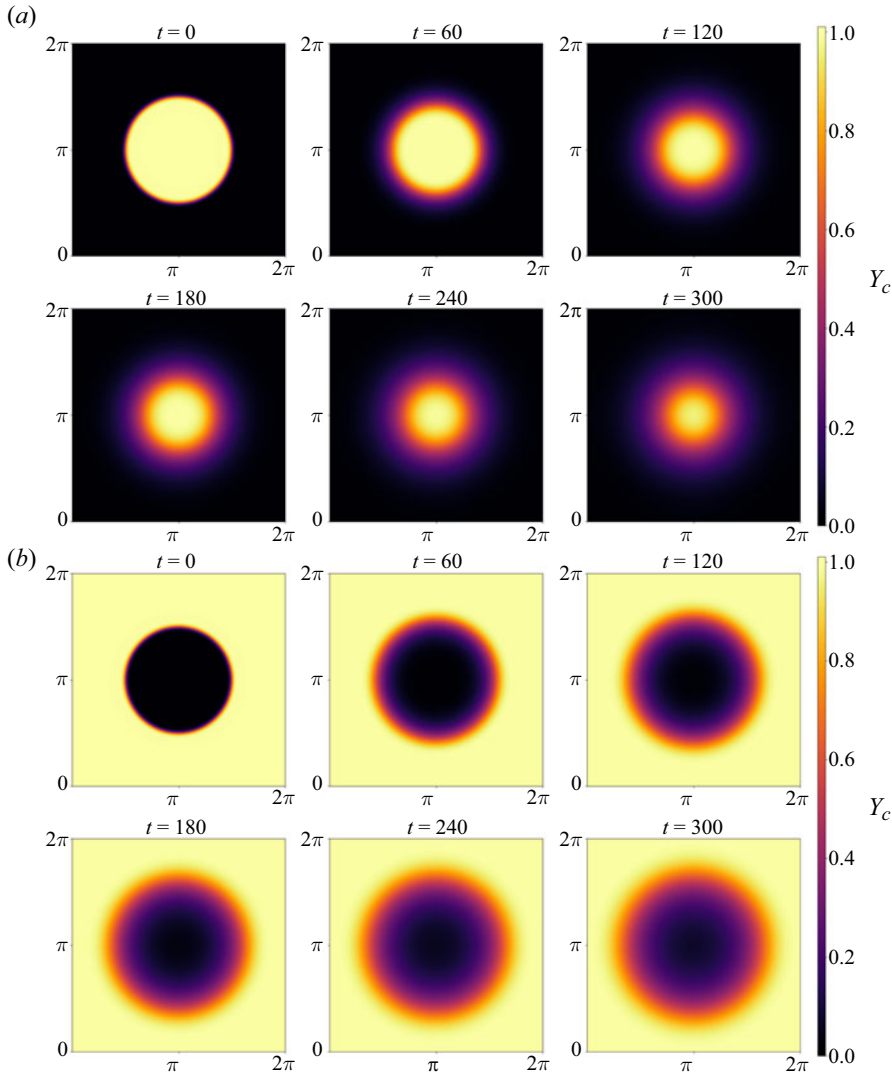
Figure 3. Contours of concentration of blob for $At = 0.5^*$ (*a*) and $At = -0.5^*$ (*b*) at same times. Darker colour indicates heavier species. The changes in concentration indicate the mixing driven solely by molecular diffusion. The lighter blob shrinks while the heavier blob expands. In the above contours, the lighter colour indicates the species which is less dense while the darker colour indicates the species which is heavier.

where from (3.3), we see that for $At = 0.5$, $\chi > 1$, $D_2 < 0$ and hence the interface moves inwards, while for $At = -0.5$, $\chi < 1$, $D_2 > 0$ and hence the interface moves outwards. Analogously, the density-driven nonlinear dissipation term alters the direction of movement of the interface based on the density gradient direction. The movement of the interface affects the decay of concentration gradients and hence we see the difference in average slopes of decay in figure 4(*a*).

Although the interface (location of $|\nabla Y_c|_{max}$) seems to expand for $At < 0$ and shrink for $At > 0$, the area where the blob species can be found (or the area occupied) identified as $Y_c > 0.01$ increases for both the cases. Figure 4(*b*) shows that the area occupied is similar for both $At < 0$ and $At > 0$, but significantly smaller than the passive scalar. In the next section, we discuss the influence of shock waves on active scalar mixing.
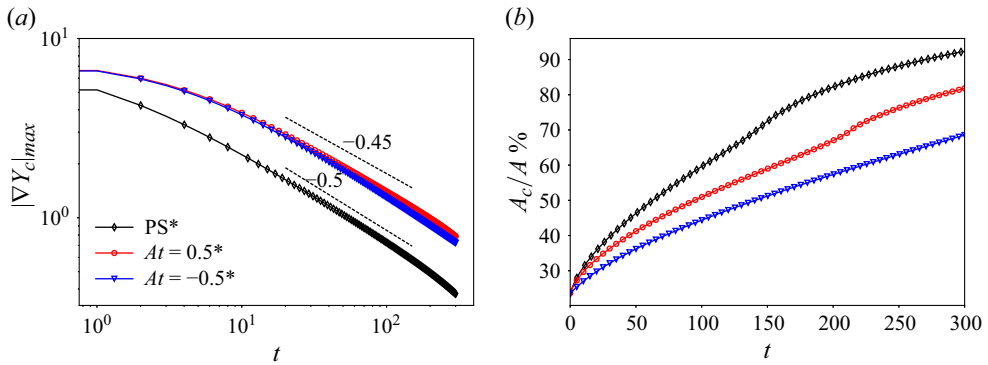
Figure 4. Evolution of maximum value of $|\nabla Y_c|$ in log–log scale with the averaged slope of decay (*a*) and evolution of the percentage of area occupied by the circular species (*b*). The presence of density gradients in active scalars alters the diffusion coefficients as shown in (3.3) compared with passive scalar diffusion, hence modifying the rate of decay.

3.2. *Stirring effect of shock waves*

Stirring increases the mean value of concentration gradients and also increases the area across which molecular diffusion occurs. Random shock waves interact with the blob interface characterised by large density gradients. Baroclinic torque generated by such interactions generates localised vorticity at the interface. Consequently, the interface deforms and folds, thus increasing the apparent perimeter over which diffusion takes place. We call this baroclinic vorticity induced mixing as stirring. In this section, we analyse the stirring action of shock waves and its role in enhancing the mixing of active scalars. We also discuss the effect of the Atwood number on the evolution of the concentration levels and present a comparison of the time scales of each mixing process. Furthermore, we distinguish between stirring-dominated and diffusion-dominated regimes of mixing by using the maximum value of species concentration.

Stochastically generated shock waves interact with the blob interface where the gradient of density is maximum. Figures 7(*a*) and 7(*b*) show the contours of the evolution of the circular species concentration for $At = 0.5$ and $At = -0.5$, respectively. In comparison with the no shock cases of figures 3(*a*) and 3(*b*), we see that in the presence of shock waves, the blob is stretched and folded leading to a continuous distortion of the interface. The figures suggest that homogenisation occurs at a faster rate under the stirring action of shock waves, resulting in a completely mixed state. To quantify the extent to which shocks enhance the mixing process, we compare the space-filling capacity of the blob species in the presence of shock waves to the no-shock cases. Figure 8(*a*) shows that shock waves increase the rate of the space-filling capacity of the blob compared with the no-shock/only molecular diffusion case. Shock waves increase the space-filling capacity by increasing the mean concentration gradients and sustaining them for a longer time as shown in figure 8(*b*). For passive scalars, shocks have a negligible effect on the mixing because the baroclinic torque is absent. We discuss the reason for the sustained gradients in the case of active scalars in detail below.

The concentration diffusion flux is proportional to the perimeter of the interface across which diffusion occurs and the strength of the gradients across the interface. As mentioned earlier, the role of stirring is to increase the perimeter, thereby increasing the total diffusion flux across the interface. This also results in an increase in the mean magnitude of concentration gradients. Figures 9(*a*) and 9(*b*) show the contours of $|\nabla Y_c|$ for positive and negative Atwood numbers, respectively. The figures also show that the mean magnitude of
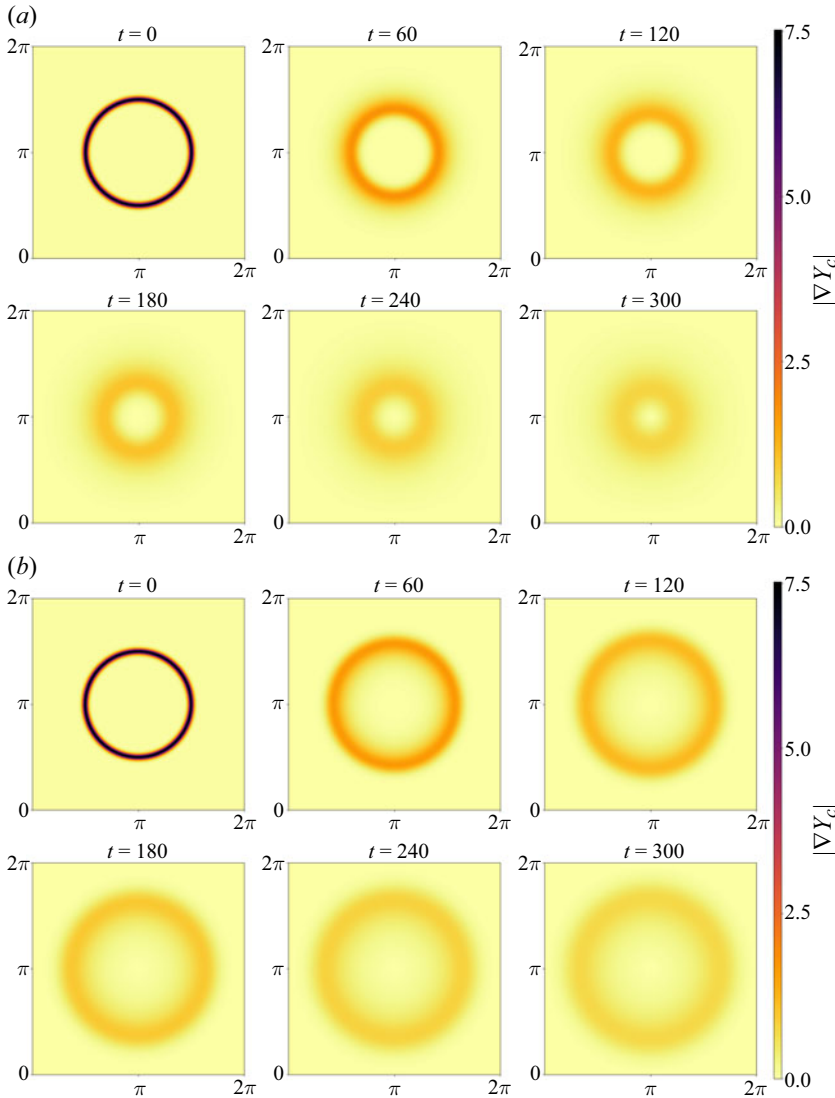
Figure 5. Contours of $|\nabla Y_c|$ for $At = 0.5^*$ (a) and $At = -0.5^*$ (b) at same times. Due to the terms II and III in (3.3), the interface moves inwards for the lighter blob while the interface moves outwards for the heavier blob.

concentration gradients ($\langle|\nabla Y_c|\rangle$) increases due to an increase in the perimeter of the blob interface caused by shock waves. Furthermore, for all the active scalar cases with shocks, we see that the concentration gradients decay faster in the final time instances when compared with the no-shock cases. Figure 9(a) shows that a lighter blob homogenises faster when compared with a denser blob. To quantify the effectiveness of stirring, we look at the mean magnitude of concentration gradient and compare it with the mixing driven by only molecular diffusion in figure 8(b). For the no-shock cases, the negative Atwood number case has a mean value that increases with time, while for the positive Atwood number case, the mean value of the concentration gradient decays with time. This is due to the nonlinear diffusive transport (termed as nonlinear dissipation) which causes the interface to expand for $At < 0$ and shrink for $At > 0$. Initially, when $Y_c \approx 1$ near the
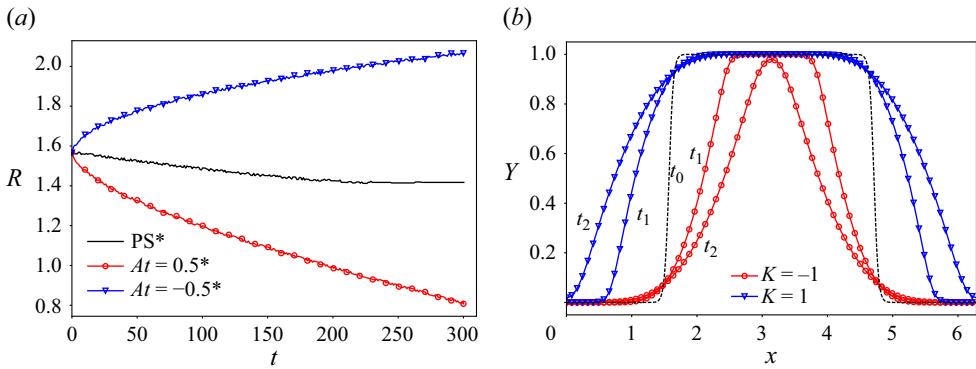
Figure 6. Evolution of the location of $|\nabla Y_c|_{max}$ measured from the centre of the blob (a) and 1-D evolution of Y from the 1-D unsteady nonlinear diffusion equation (3.5) solved using a 1-D Fourier pseudospectral solver (b). The directions of concentration and density gradients affect the coefficients of terms II and III in (3.3), causing the interface of the positive Atwood case to move inwards and the negative Atwood case to move outwards. The black line represents the initial condition at $t = t_0$. The blue and red lines represent cases with $K = \pm 1$, respectively, and $t_0 < t_1 < t_2$. For $K > 0$, the interface moves outwards while diffusing and for $K < 0$, the interface moves inwards while diffusing.

interface, the denser blob ($At < 0$) tends to expand quickly compared with diffusion, and *vice versa* for the lighter blob ($At > 0$). This can be realised by considering the ratio of the molecular diffusion time scale (τ_m) to the nonlinear dissipation time scale (τ_d) given as

$$\frac{\tau_m}{\tau_d} \sim \frac{|D_2|}{D_1} \sim \frac{|1 - \chi|}{1 + (\chi - 1) Y_c}. \tag{3.6}$$

The reader is referred to appendix B for a detailed discussion on the ratio of the molecular diffusion time scale to the nonlinear dissipation time scale.

Figure 8(b) shows that the shock waves increase the mean magnitude of concentration gradients for the Atwood numbers cases. However, the passive scalar concentration gradient is not affected by the shock waves. Figure 10 shows that shock waves increase the mean magnitude of the concentration gradients for all Atwood numbers considered by increasing the area (apparent perimeter in two dimensions) across which the gradients are present. Figure 10 also shows that the negative Atwood numbers attain a higher value of $\langle|\nabla Y_c|\rangle$ than the positive Atwood numbers. Though the diffusion term smoothens out the gradients and reduces the value of the concentration gradients in all Atwood number cases locally, the increase in the mean magnitude is due to the increase in the perimeter. The outwards expansion in the negative Atwood number cases further increases the perimeter and causes the gradients to exist over a larger perimeter. Additionally, as the magnitude of the Atwood number increases, more stretching and folding of the interface occurs thus increasing the generated maximum mean concentration gradients.

Figure 11 shows the evolution of maximum value of $|\nabla Y_c|$ for passive and active scalar cases with shocks. We see that the dynamics of the passive scalar case with and without shocks are similar. A few fluctuations in the maximum value of $|\nabla Y_c|$ exist which can be attributed to the randomised vorticity generated due to the curvature of the randomly generated shocks (Jossy & Gupta 2023). The maximum value of $|\nabla Y_c|$ also decays for the active scalar cases but with localised random spikes in values. The presence of shock waves sustains the gradients longer for the active scalar cases. We quantify this through figures 12(a) and 12(b), which show the PDF of the magnitude of concentration gradients
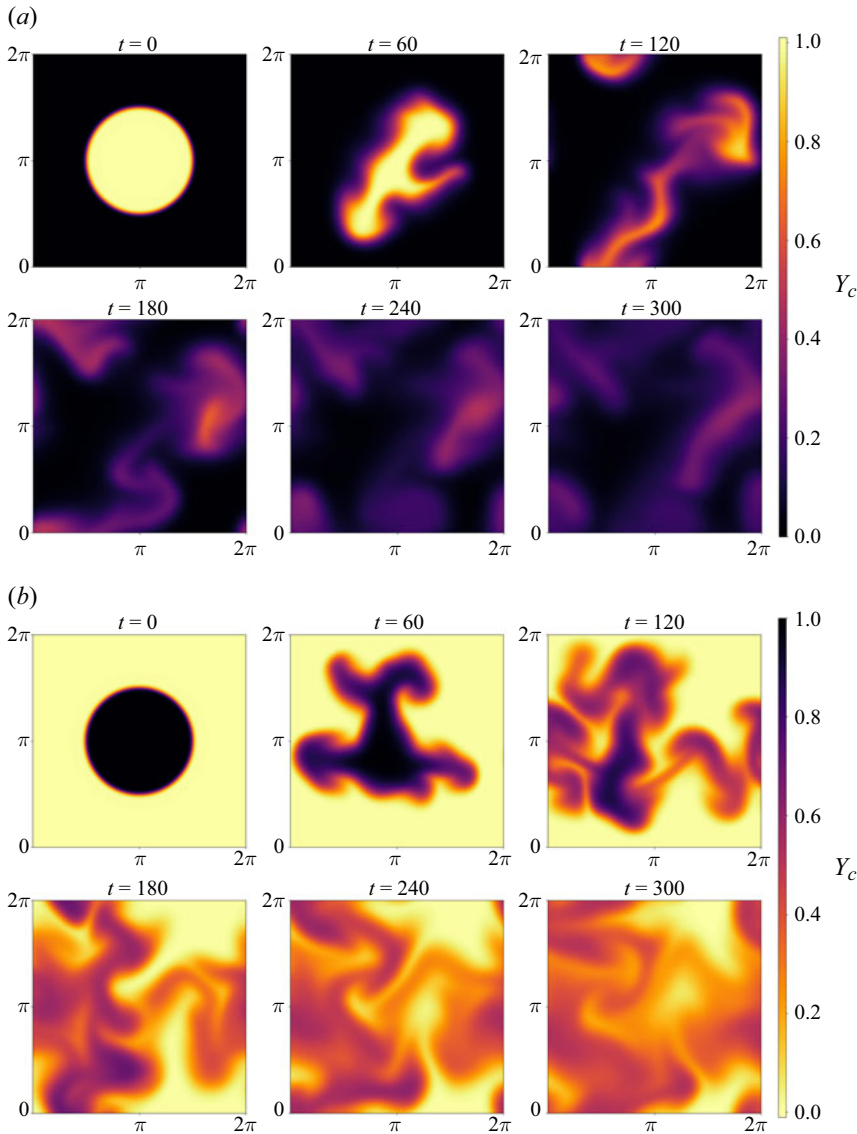
Figure 7. Contours of concentration of blob for $At = 0.5$ (a) and $At = -0.5$ (b) at same times. The darker colour indicates heavier species. A comparison with figures 6(a) and 6(b) shows that shock waves enhance the mixing process. Shock waves continuously deform the interface of the blob, breaking it apart. The denser mixture (lighter blob) homogenises faster than the lighter mixture (denser blob). In the above contours, the lighter colour indicates the species that is less dense while the darker colour indicates the species that is heavier.

for $At = 0.5$ and $At = -0.5$, respectively. We observe that the decay of the tail is more rapid for $At > 0$ compared with $At < 0$.

The above discussion indicates towards two regimes of mixing: one where the action of stirring is dominant (termed as the vorticity-dominated regime) and the other where molecular diffusion is dominant (termed as the diffusive regime). The regime to the left of the peak value of $\langle |\nabla Y_c| \rangle$ in figure 10 is the vorticity-dominated regime, and the regime to the right is the diffusive regime. In the vorticity-dominated regime, the interface gets stretched and folded due to baroclinic vorticity (also discussed in § 3.3).
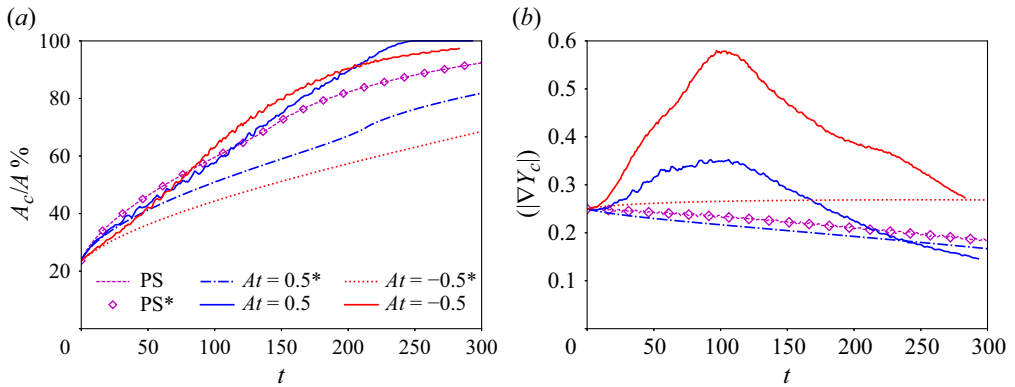
Figure 8. Evolution of percentage of the ratio of mixed area to total area (*a*) and the evolution of area-averaged concentration gradients (*b*). Shock waves improve the space-filling capacity of active scalars when compared with the pure diffusion cases. The labels are identical for both the figures.

As the stretching continues, more points inside the blob are exposed to the surrounding species, thus facilitating molecular diffusion more. As we discuss below, for $At < 0$, the interface keeps expanding, thus delaying the time taken by stirring to expose all the points inside the blob to the surrounding species.

To estimate the time until which the interface of the blob can be stretched, we calculate the normalised maximum concentration (Y_c^N) given by

$$Y_c^N = \frac{Y_{c,max}}{Y_{c,max}^0}, \tag{3.7}$$

where $Y_{c,max}$ is the maximum concentration of the circular species at the given instant and $Y_{c,max}^0$ is the initial maximum concentration of the circular species. The normalised maximum concentration has been used to estimate the mixing time in passive scalar mixing (Meunier & Villermaux 2003) and shock–bubble interaction mixing (Liu *et al.* 2022) studies. A normalised maximum concentration (Y_c^N) <1 indicates that stirring has stretched the blob interface and exposed all of it to the surrounding species. After this instant, the role of stirring is secondary and the molecular diffusion dominates. For positive Atwood numbers, the nonlinear dissipation results in the apparent contraction of the blob. Hence, the overall time taken to expose all the points of the blob species to the surroundings is smaller. However, for negative Atwood numbers, the effect of the outwards expansion delays the time taken for all points of the blob to be exposed to the surrounding species. To account for the outwards expansion, we modify the normalised maximum concentration as follows for negative Atwood number cases:

$$Y_c^N = \frac{Y_{c,max}}{0.95 \ Y_{c,max}^0}. \tag{3.8}$$

The vertical lines on figure 10 indicate the time when normalised maximum concentration falls below unity. We see that the estimated time is located very close to the peaks of $\langle |\nabla Y_c| \rangle$. Hence, the calculated normalised maximum concentration highlights that stirring deforms any geometrical concentration inhomogeneity until all the points of the inhomogeneity are exposed to stronger gradients. Therefore, it serves as a suitable indicator for distinguishing the regimes where stirring and molecular diffusion are dominant. In the next section, we discuss the role of baroclinic vorticity and also its role in increasing the stirring time of a denser blob.
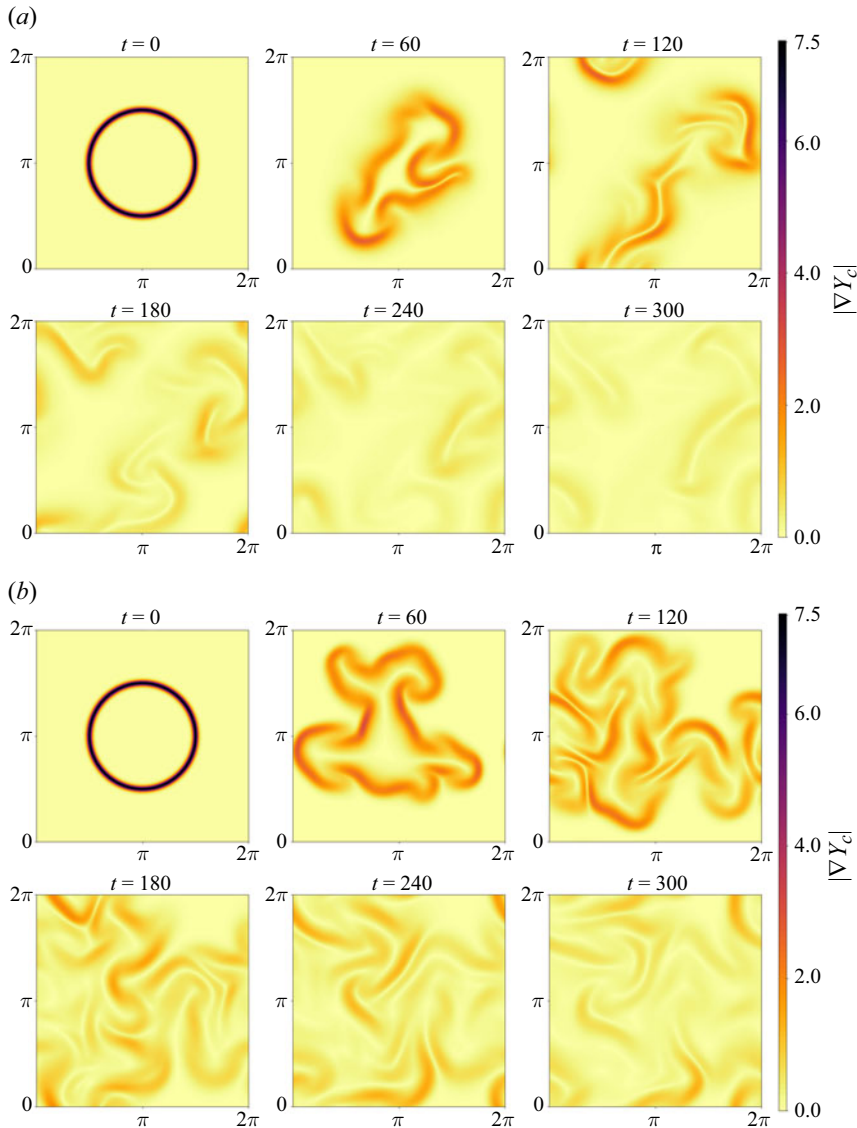
Figure 9. Contours of $|\nabla Y_c|$ for $At = 0.5$ (*a*) and $At = -0.5$ (*b*) at the same times. The concentration gradients are sustained longer for the denser blob. This is due to the outwards expansion of interface by the terms II and III in (3.3) which delays the exposure of the blob to the action of molecular diffusion.

3.3. *Role of baroclinicity in stirring*

In this section, we discuss the mechanism by which the stirring action of the randomly generated shock waves increases the apparent interfacial perimeter. We show the effect of the Atwood number on baroclinicity and its role in enhancing the mixing. We also derive a time scale for the shock-induced stirring and show that it is sustained for a longer time for a lighter mixture.

As discussed in the previous section, the presence of shock waves increases the mean magnitude of concentration gradients for active scalars. But, figure 8(*b*) shows that, despite the presence of shocks, the mean magnitude of the concentration gradients for the passive
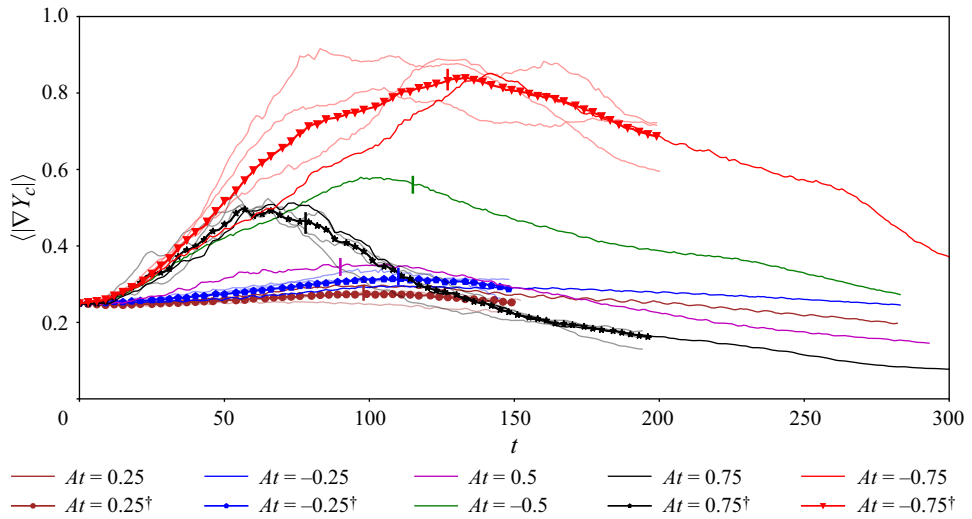
Figure 10. The evolution of area-averaged concentration gradients. The vertical lines indicate the mixing time calculated using (3.7) and (3.8) for positive and negative Atwood numbers, respectively. The labels are identical for both the figures.
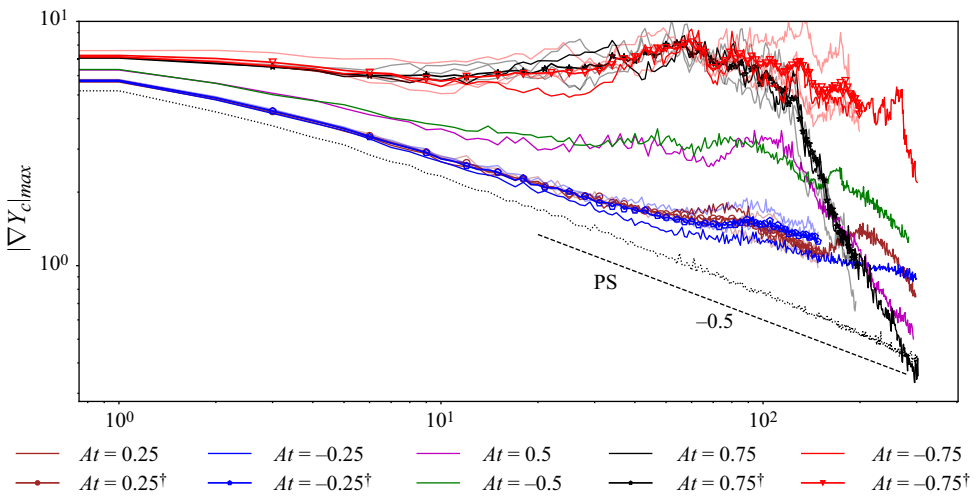

Figure 11. Evolution of maximum value of $|\nabla Y_c|$ in log–log scale for all the cases in table 2. Shock waves have no significant effect on the decay of the maximum concentration gradients of passive scalars. The presence of density gradients in active scalars sustains concentration gradients longer compared with the passive scalar.

scalar does not increase. The stirring action of shock waves affects mixing through the advection term of the species equation in (2.4). The velocity in the advection term can be decomposed using Helmholtz decomposition as follows:

$$\boldsymbol{u} = \boldsymbol{u_w} + \boldsymbol{u_v} \tag{3.9}$$

where $\boldsymbol{u_w}$ and $\boldsymbol{u_v}$ are the acoustical and vortical components of velocity, respectively. Both passive and active scalars have the same rate of injection of acoustical energy. Therefore,
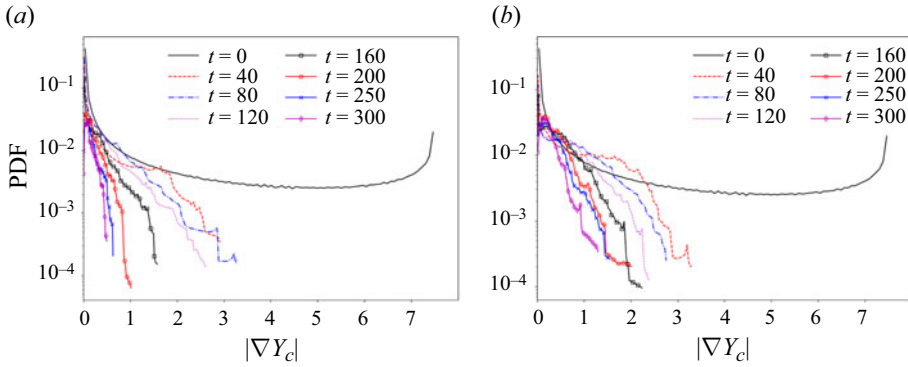
1007 A25-20

Figure 12. The PDF of the magnitude of concentration gradient at different time instances for $At = 0.5$ (*a*) and $At = -0.5$ (*b*). Initially, the PDF indicates two peaks, one at 0 and other at the maximum value inside the interface. With time, the PDF tails drop indicating diffusion. Negative Atwood numbers sustain concentration gradients longer owing to the outwards expansion effect of the nonlinear dissipation terms.

any difference caused between the two would stem from the vortical component of velocity ($\boldsymbol{u_v}$). We obtain the evolution equation of vorticity ($\boldsymbol{\omega}$) by taking the curl of (2.2) as

$$\frac{\partial \boldsymbol{\omega}}{\partial t} = \frac{\boldsymbol{\nabla}\rho \times \boldsymbol{\nabla} p}{\rho^2} + \frac{\mu \nabla^2 \boldsymbol{\omega}}{\rho Re_{ac}} + \frac{\mu}{Re_{ac}} \frac{\boldsymbol{\nabla}\rho \times [\boldsymbol{\nabla} \times \boldsymbol{\omega}]}{\rho^2}$$
$$- \left(\frac{4\mu}{3Re_{ac}}\right) \frac{\boldsymbol{\nabla}\rho \times \boldsymbol{\nabla}(\boldsymbol{\nabla} \cdot \boldsymbol{u})}{\rho^2} - \boldsymbol{\nabla} \cdot (\boldsymbol{u}\boldsymbol{\omega}) + \boldsymbol{F_{\omega}^r}. \tag{3.10}$$

The last term on the right-hand side of (3.10) is the vortical forcing component and is zero in the current study. The first term on the right-hand side is the baroclinic term and is the primary term responsible for generation of vorticity in the domain, and hence the stirring action. The behaviour of the diffusion terms of vorticity is similar to the findings reported earlier (Jossy & Gupta 2023), where the interaction of random shock waves with thermal gradients was analysed. The second term is the viscous diffusion of vorticity and is the major contributor to the vorticity dissipation. The next two terms represent the interaction of density gradients with viscous stresses in the domain. The term proportional to bulk force ($\boldsymbol{\nabla}(\boldsymbol{\nabla} \cdot \boldsymbol{u})$) has higher dissipation contribution than the dissipation term propositional to the shear stress ($\boldsymbol{\nabla} \times \boldsymbol{\omega}$) in a flow field where shocks are involved. The term proportional to bulk force will be maximum along the shocks where the divergence of velocity is maximum. These terms will increase in magnitude with increase in Atwood number, due to stronger density gradients. The second last term is the advection term of vorticity, which has the minimum contribution to the enstrophy budgets (Jossy & Gupta 2023).

The difference between passive and active scalars is the presence of the density gradients in the latter. In our study, vorticity production is primarily due to the misalignment of the pressure gradients in the shock waves and the density gradients at the blob interface. This indicates that the absence of strong density gradients in the passive scalar case results in no stirring effect. The mixing of both active and passive scalars is primarily due to the vortical (solenoidal) structures and is independent of compressibility when it comes to large-scale effects. Similar observations were made in the compressible mixing of passive scalars, where the dilational component did not enhance the mixing process of passive scalars (John *et al.* 2019; Ni 2016). Jossy & Gupta (2023) show that shock waves generated by
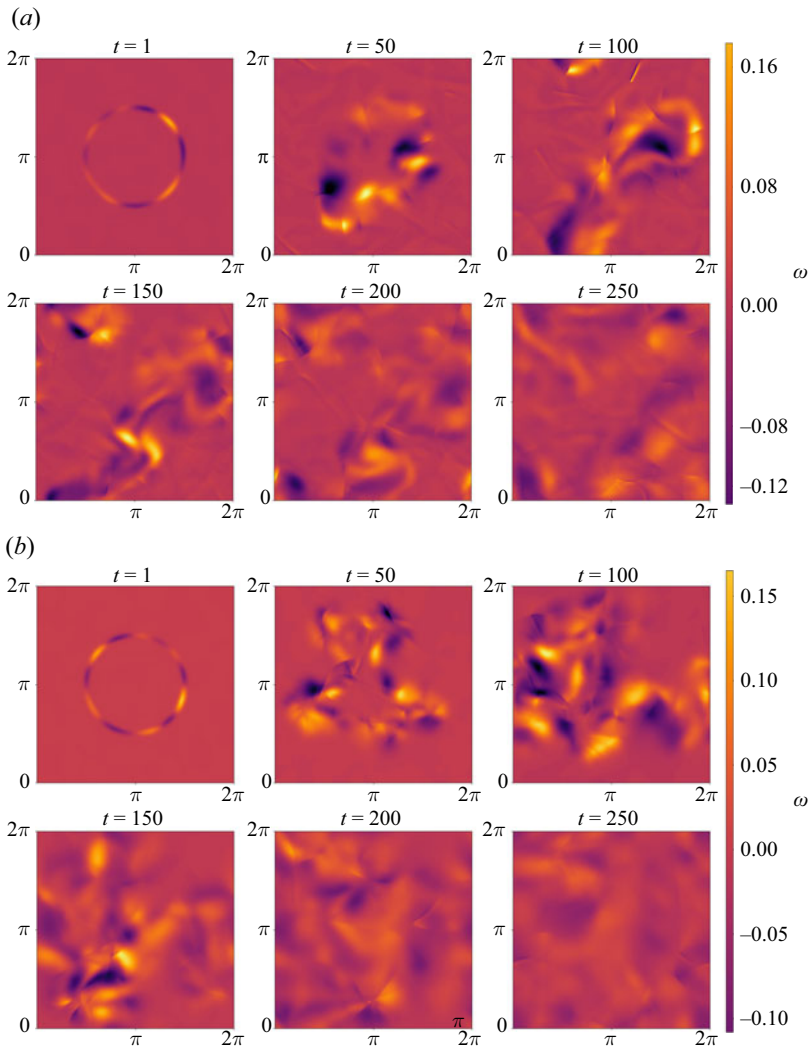
Figure 13. Contours of vorticity for $At = 0.5$ (*a*) and $At = -0.5$ (*b*) at the same times. The vorticity is concentrated along the perimeter where density gradients are maximum with alternating rotating and counter-rotating vortices. Spikes and bubbles develop at the intersection of the vortices rotating in opposite directions.

stochastic forcing generate broadband vorticity owing to the continuous variation of shock curvature. We see that vorticity generated due to shock curvature has only a slight and insignificant effect on the mixing of passive scalars. Hence, the vorticity generated at the interface between the blob and surrounding species is solely responsible for mixing of the active scalars.

Figures 13(*a*) and 13(*b*) show the vorticity contours of $At = 0.5$ and $At = -0.5$, respectively. We see that the vorticity is concentrated along the interface of the blob. As discussed earlier, the only source of production of strong vorticity in a two-dimensional compressible flow in a periodic domain is baroclinicity. The pressure gradients within the shock waves and the high-density gradients along the interface of the inhomogeneity result in vorticity production due to baroclinicity. In this context, the current study resembles a continuously forced RMI set-up (Richtmyer 1954; Meshkov 1969), where shock waves

1007 A25-22

are continuously distorting the interface at random locations and random time intervals governed by the stochastic forcing of the shock waves. Similar to RMI, we see the development of spikes (denser fluid penetrating into lighter fluid) and bubbles (lighter fluid penetrating into denser fluid) at the interface (Abarzhi 2002; Yuan *et al.* 2023). Figures 13(*a*) and 13(*b*) show that both clockwise and anticlockwise rotating vortices are present along the interface of the blob and surrounding species. The resultant direction of velocity at each intersection of clockwise rotating vortices and anticlockwise rotating vortices results in either the production of a spike or a bubble. This results in the stretching of the interface in addition to the stretching (compression) occurring from the nonlinear dissipation terms for a denser (lighter) blob (as highlighted in § 3.1). The sharp jump in tangential velocity across the interface can also trigger shear instability, a KHI in the limiting inviscid case. Such a shear instability results in further folding of the interface. However, in the current study, it is difficult to distinguish between the role of RMI and KHI in enhancing the mixing due to the continuous forcing of the RMI. We also see a reduction in the vorticity production with time. This is expected as the mixing in active scalars proceeds to homogenise density gradients, thus reducing the magnitude of baroclinic torque generated due to the interaction of shock waves. Note that the shock waves are continuously forced, and hence typical values of ∇p remain similar as indicated by figure 2(*b*). The strength of the shock waves can be altered by changing the rate of energy injection ε in (2.13). Any reduction in the rate of energy injection will reduce the strength of the shock waves, leading to a weaker baroclinic vorticity. This will result in the species taking a longer time to homogenise. In a similar fashion, any increase in the rate of energy injection will result in stronger shocks leading to faster homogenisation.

At the initialisation, the magnitude of the density gradient increases with the absolute value of the Atwood number due to the increasing density difference. Stronger density gradients produce higher values of baroclinic vorticity. Figure 14(*a*) shows the evolution of the magnitude of the area-averaged baroclinic vorticity generation for all the active scalar cases with shock waves. We see that the baroclinicity increases with a wider disparity in density ratio between the surrounding and the circular species. The increase in baroclinicity indicates an increasing amount of stirring. Furthermore, prolonged high values of baroclinicity indicate prolonged stirring, which is the case for $At < 0$ mixtures. Figure 14(*a*) suggests that baroclinicity is responsible for stretching the interface and that the stretching is higher for larger absolute values of the Atwood number. To show that the stretching of the interface is primarily due to stirring and not the nonlinear dissipation terms, we compare their respective time scales. We derive the time scale for stirring from the evolution equation for the advection term of the species equation, which is given by

$$\frac{\partial Y_k}{\partial t} = \boldsymbol{u_v} \cdot \nabla Y_k. \tag{3.11}$$

Using scaling arguments, the time scale of stirring τ_s can be written as

$$\frac{1}{\tau_s} \sim \left(\frac{L_v}{\tau_v}\right) \frac{1}{L}, \tag{3.12}$$

where τ_v is the vortical time scale, L is the length scale across which the concentration change occurs and L_v is the vortical length scale. Both L and L_v are of the same order since any changes in the concentration from stirring occur only where vorticity is present. To derive the vortical time scale, we use the vorticity equation with only baroclinic term

$$\frac{\partial \boldsymbol{\omega}}{\partial t} = \frac{\nabla p \times \nabla \rho}{\rho^2}, \tag{3.13}$$
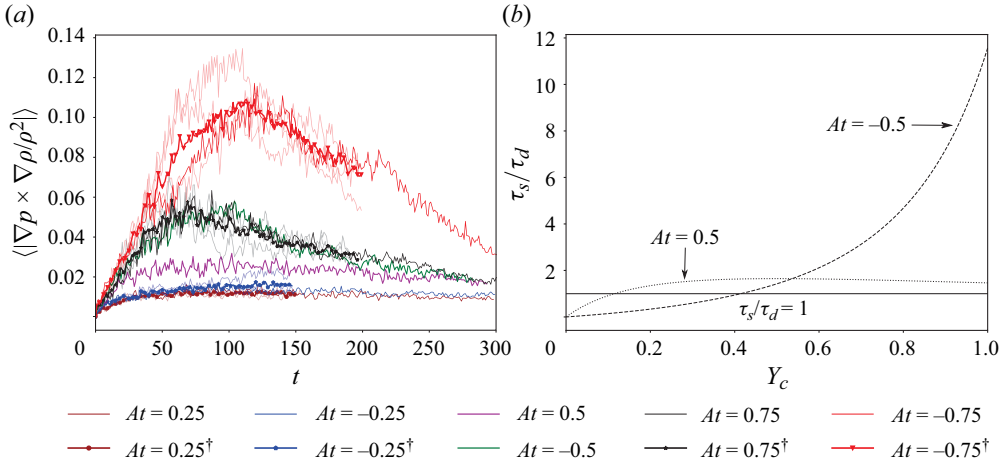
Figure 14. Evolution of the area-averaged magnitude of baroclinic vorticity generation (*a*) and the variation of the ratio of the time scale of stirring to nonlinear dissipation with a concentration level of blob (*b*). The wider disparity in density ratios results in stronger baroclinic vorticity production. The stronger vorticity is responsible for stretching the perimeter of the interface.

from which we obtain

$$\frac{c_m}{\ell} \frac{1}{\tau_v} \sim \frac{\left(\frac{\Delta p}{\eta}\right)\left(\frac{\Delta \rho}{\delta}\right)}{\rho_m^2}, \tag{3.14}$$

where ℓ/c_m is the time scale of the passage of a shock wave and ρ_m is the total density of the mixture. The pressure jump Δp is estimated using the mean Mach number of the shock waves and $\Delta \rho$ is a function of the Atwood number. In a similar fashion, we derive the time scale of the nonlinear dissipation term from

$$\frac{\partial Y_k}{\partial t} = \frac{D_2}{Re_{ac}Sc} \left(\nabla Y_k \cdot \nabla Y_k\right). \tag{3.15}$$

The time scale of the nonlinear dissipation is obtained as

$$\frac{1}{\tau_d} \sim \frac{|D_2|Y_c}{Re_{ac}ScL^2}. \tag{3.16}$$

Using (3.12), (3.14) and (3.16) we get a comparison of the time scales of nonlinear dissipation and stirring as

$$\frac{\tau_s}{\tau_d} \sim \frac{|D_2|Y_c}{Re_{ac}ScL^2} \frac{\rho_m^2}{\left(\frac{\Delta p}{\eta}\right)\left(\frac{\Delta \rho}{\delta}\right)} \frac{c_m}{\ell}. \tag{3.17}$$

Figure 14(*b*) shows the variation of the ratio of stirring time scale to the nonlinear dissipation with concentration levels of the blob. We note that for typical values of Y_c at the interface $0 < Y_c < 1$, the stirring time scale is slower than the dissipation time scale $\tau_s/\tau_d > 1$ for all Atwood numbers. For higher values of Y_c, the stirring is considerably slower than dissipation for $At < 0$ (denser blob, lighter mixture) as compared with $At > 0$ (lighter blob, denser mixture). In the initial stages, for high values of Y_c inside the interface, the lighter inhomogeneities tend to get mixed by the shocks earlier than the denser inhomogeneities (also see $t = 1$ vorticity contours for $At = 0.5$ and $At = -0.5$ mixtures in figure 13), As the maximum value of Y_c decreases due to mixing, stirring
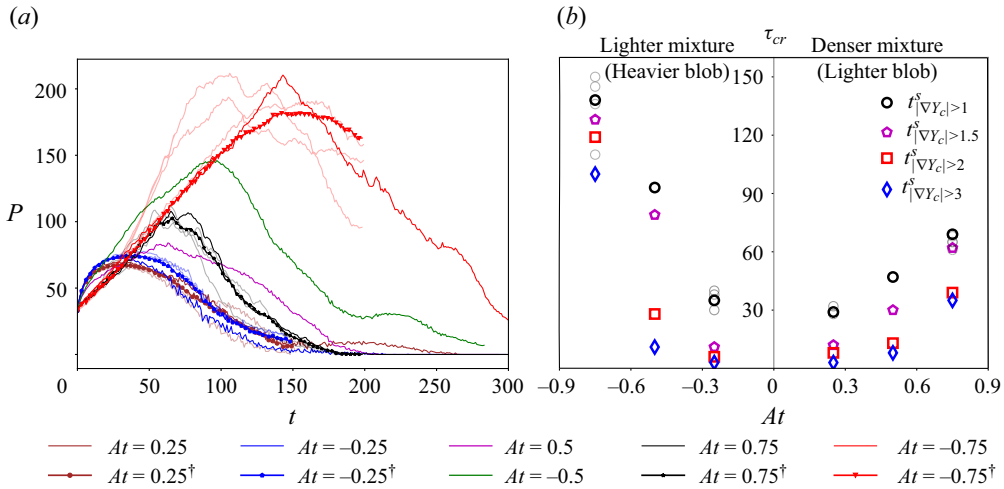
1007 A25-24

Figure 15. Evolution of the apparent interface perimeter obtained by using the condition $|\nabla Y_c| > 1.0$ (*a*) and the critical time of occurrence of maximum value of perimeter versus Atwood numbers (*b*). Shock waves stretch the interface across which molecular diffusion occurs, allowing more molecular diffusion to occur. The superscript *s* stands for the maximum time taken to reach peak perimeter for the simulations by stirring, and the subscripts indicates the value of ∇Y_c used to track the perimeter. The trend of the critical time is independent of the choice of the limiting value of ∇Y_c used for calculating the interface.

becomes faster than the nonlinear dissipation for denser inhomogeneities, indicating dominant stirring action at later stages for $At < 0$ mixtures.

We have shown that the baroclinicity is responsible for enhancing the mixing by stretching the interface of the blob. As mentioned earlier, it is difficult to track any definite interface to calculate the perimeter. But to show the effect of baroclinicity, we calculate a characteristic apparent perimeter (P) by tracking the area defined by $|\nabla Y_c| > 1$ and dividing it by the initial characteristic width (δ in (2.13)). Figure 15(*a*) shows the evolution of the apparent perimeter of all the active scalar cases with shock waves. We see that the perimeter for the active scalars increases with an increase in baroclinicity. The peak value of the perimeter shifts to the right with an increase in the absolute value of the Atwood number. The shift is more for a heavier blob when compared with a lighter blob, as the increase in the perimeter is augmented by the outwards expansion due to the nonlinear dissipation terms. Moreover, the time of occurrence of the maximum value of the perimeter (τ_{cr}) depends on the choice of the limiting value of $|\nabla Y_c|$ used to identify the interface for the apparent perimeter calculation. However, the trend of τ_{cr} remains identical for any choice of the limiting value provided the limiting value is not the characteristic value of the concentration gradient in the diffusive regime ($Y_c^N < 1$). Figure 15(*b*) shows the occurrence of the time at which maximum perimeter is achieved for different choices of $|\nabla Y_c|$. The maximum time (τ_{cr}) is labelled as the critical time as it distinguishes the time before which the action of stirring is dominant over molecular diffusion. We see that the $At < 0$ mixtures (heavier blob, lighter mixture) have a longer stirring time than $At > 0$ mixtures (lighter blob, denser mixture). The trend remains the same irrespective of the choice of interface parameter. The simulation results are in line with the time scale analysis, which shows that the stirring action is sustained longer for the $At < 0$ mixtures. The current two-dimensional study isolates the mixing effects of the vorticity by baroclinicity. In three-dimensional cases, the mixing effects will be further enhanced by the vortex stretching mechanism.
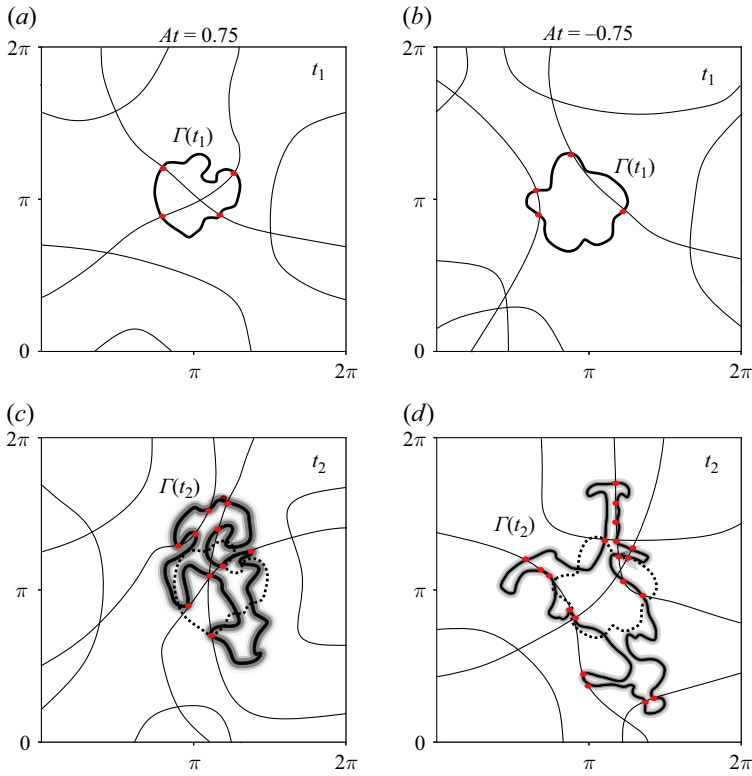
Figure 16. Schematic illustrating the interaction of forced periodic shock waves with the concentration interface for $At = 0.75 (a,c)$ and $At = -0.75$ (b,d) cases at time t_1 (a,b) and a later time t_2 (c,d). The shocks were traced and sketched using the dilatation values and the interface was traced and sketched using the magnitude of the concentration gradient. As the interface is stretched and folded by the baroclinic vorticity, more interaction points are introduced thus resulting in increased baroclinic interactions. This stretching is augmented by the interface expansion in the $At < 0$ case due to the nonlinear dissipation term, further increasing the baroclinic interactions.

In figure 15, we note that higher variation occurs in critical time values for the negative Atwood numbers' stochastic realisations when compared with that of the positive Atwood numbers. The same can also be inferred from figure 14(a), where the area-averaged baroclinicity shows that the vorticity generated has a higher degree of variation for negative Atwood numbers for different stochastic realisations at the same Atwood number. We explain this difference using the schematic shown in figure 16. Figures 13(a) and 13(b) show that baroclinic vorticity is of significance only at the interface where the high-pressure gradients within the shock waves interact with the high-density gradients present across the interface. Figures 16(a) and 16(b) illustrate this interaction at some initial time t_1. Figures 16(a) and 16(b) also highlight the points of interaction between the shock waves and the density gradients across the interface. Therefore, the vorticity generated due to baroclinicity is the summation of N such interactions across the interface (Γ). This can be expressed as

$$\left\langle \left| \frac{\nabla \rho \times \nabla p}{\rho^2} \right| \right\rangle \approx \oint_{interface} \left| \frac{\nabla p \times \nabla \rho}{\rho^2} \right| d\Gamma \approx \sum_{i=1}^{N} \left| \frac{\nabla p \times \nabla \rho}{\rho^2} \right|_i \Delta \Gamma_i, \qquad (3.18)$$

where the pressure gradient at each point of interaction is a stochastic process and has a variance associated with it. At a later time, t_2, the perimeter of the interface is stretched by the baroclinic vorticity for both positive and negative Atwood number cases. The same is also shown in schematic figures 16(*c*) and 16(*d*). However, the perimeter is higher for the negative Atwood number cases compared with the positive Atwood number case due to the nonlinear dissipation term. The increase in perimeter results in more points of interaction between the pressure gradients and density gradients, resulting in more baroclinic vorticity. This indicates that for identical parameters of stochastic forcing, the negative Atwood number cases will generate more vorticity than the positive Atwood number case for the same magnitude of density gradients across the interface, and the same can also be seen in figure 14(*a*). This increase in the number of interaction points also increases the uncertainty/variance associated with pressure gradients across the interface. Negative Atwood numbers have more such points when compared with positive Atwood numbers, and hence have more variation in values among realisations. But at later times, when molecular diffusion dominates mixing, the variance among realisations reduces.

4. Conclusions

We have studied the enhancement of the mixing of an active scalar by the stirring action of stochastically forced shock waves using two-dimensional DNS. We consider the mixing of two different species of varying densities where one of the species has an initial circular profile. The Atwood number is used as the dimensionless parameter to study the effect of the shock waves on the mixing of a lighter blob ($At > 0$) and a denser blob ($At < 0$). We simplify the diffusion term in the evolution equation for the concentration of the blob (3.3) in terms of the concentration gradients. Comparison of the diffusion terms in the concentration of passive and active scalars shows that two additional terms – concentration gradient driven nonlinear dissipation and density gradient driven nonlinear dissipation term –are present in the diffusion of active scalars in addition to the Laplacian term. We show how the presence of density gradients affects mixing by considering cases where mixing is purely due to molecular diffusion. We show that the density gradients and the concentration gradients alter the coefficients of the Laplacian term and the nonlinear dissipation terms. A 1-D unsteady nonlinear diffusion equation is used to show that the positive coefficients for the nonlinear dissipation terms for a denser blob causes the interface to expand, while the negative coefficients which occur for a lighter blob causes the interface to shrink. This competing effect of nonlinear dissipation in active scalars also modifies the effect of shock waves driven stirring on the mixing of active scalars.

We show that the stirring action of shock waves increases the space-filling capacity of the active scalars and enhances mixing overall. Shock waves increase the mean value of concentration gradients and sustain them for longer times, allowing for more effective mixing. The lighter mixtures ($At < 0$) sustain concentration gradients longer than the denser mixtures ($At > 0$) due to the perimeter increase caused by the nonlinear dissipation terms, and the time scale of this perimeter increase is similar to the shock-wave-driven stirring time scale. Shock waves enhance mixing by stretching the interface across which the molecular diffusion occurs and act until all the points of the inhomogeneity are exposed to the surrounding species. We give an estimate of this mixing time using the maximum concentration of the blob and show that it is also the time instant at which the area-averaged magnitude of the concentration gradients peaks. For compressible flow in a

two-dimensional periodic domain, baroclinicity is the only vorticity production possible, thus affecting the velocity in the advection term of the species concentration evolution equation. The interface between the active scalars exhibits large density gradients. Consequently, random shock waves interacting with this interface generate strong vorticity at the interface via the baroclinicity. Hence, a random shock field enhances the mixing of active scalars but has no effect on passive scalar mixing. We also show that the increase in density gradient increases the baroclinicity, thereby enhancing the mixing. Furthermore, shock waves do not enhance the mixing of passive scalars due to the absence of density gradients.

The current study shows that the mixing of active scalars differs significantly from that of passive scalars. In active scalar mixing, the nonlinear diffusion (termed as nonlinear dissipation in this work), the Laplacian diffusion and the stirring interplay, thus resulting in different mixing dynamics for heavier mixtures with lighter inhomogeneities as opposed to the lighter mixtures. The study is also a step towards a better understanding of shock-enhanced fuel–air mixing in air-breathing engines where there is very little residence time (Broadwell & Breidenthal 1984; Tian *et al.* 2017; Wong *et al.* 2022). The future research direction of this work is to consider the effect of the vortex stretching term in sustained three-dimensional shock-resolved simulations. In three dimensions, the higher baroclinic torque in $At < 0$ mixtures may result in the triggering of hydrodynamic turbulence, which could result in the enhancement of mixing. However, the interplay of stirring with the nonlinear diffusion of the active scalars would result in similar dynamics presented in this work.

Appendix A. Modal Convergence

To highlight the spatial convergence at $k_{max} = 1024$, we present the additional cases with $k_{max} = 768$ and $k_{max} = 1536$ (see table 2) for the positive Atwood number cases. We choose to study the convergence only for the positive Atwood number cases as they generate more scales when compared with the negative Atwood number cases (see figure 1a). Figure 17(a) shows the wave energy spectra for the different resolution cases. We see that the passive scalar cases are fully resolved for all three resolutions. As shown earlier in § 3.3, no mixing occurs in passive scalar cases. Hence, no new scales are generated as a result of mixing. Any scale that is generated is only due to wave steepening. This shows that for the given forcing parameters, the shock waves generated are completely resolved. For active scalar cases, we see that spectra for $k_{max} = 1024$ and $k_{max} = 1536$ overlap for all the cases until the dealiasing limit of $k\ell = 1024\ell$. $At = 0.25$ and $At = 0.25^{\ddagger}$ as well as $At = 0.5$ and $At = 0.5^{\ddagger}$ cases overlap for all the length scales with only a small deviation between $At = 0.75$ and $At = 0.75^{\ddagger}$ for $k\ell > 1024\ell$. Figure 17(b) shows the spectral flux of all the cases. We see that for $k_{max} = 1024$ and $k_{max} = 1536$, values overlap for all the cases, highlighting that the nonlinear terms are converged at $k_{max} = 1024$ for these cases. Additionally, we see that the spectral flux for $k\ell > 1024\ell$ is negligible for all cases, indicating that nonlinear terms are negligible for those scales and the dissipation dominates relatively. To check the resolution of dissipation dominated scales, we use the
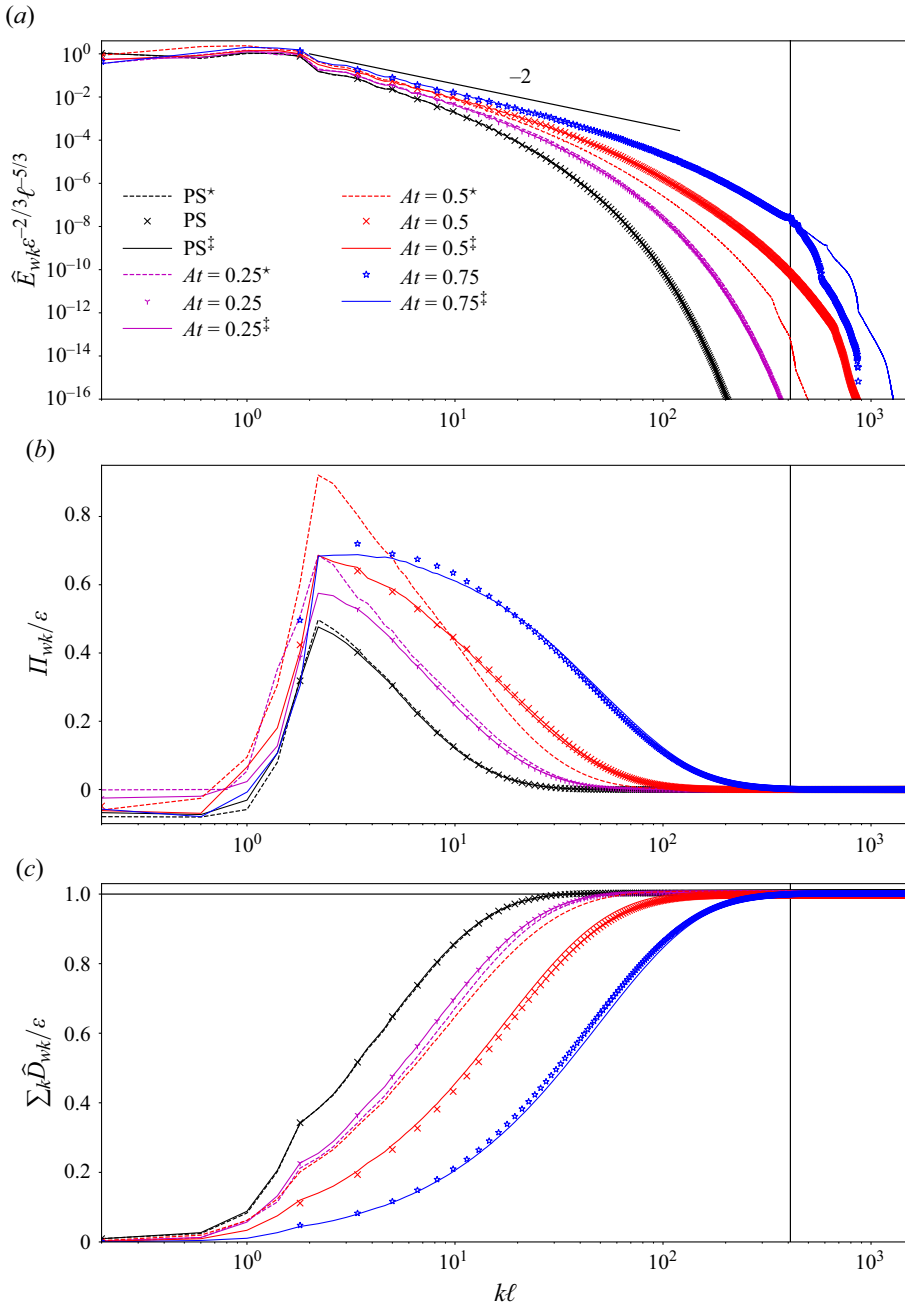
Figure 17. Dimensionless scaled density-weighted wave energy $\hat{E}_{wk}$ spectra (*a*), spectral flux of wave energy $\widehat{\Pi}_{wk}$ (*b*) and cumulative dissipation $\widehat{D}_{wk}$ (*c*). The vertical lines in the figures show the dealiasing limit $k_{max}\ell$ for $k_{max} = 1024$ cases. The spectral flux is negligible beyond the 1024ℓ limit highlighting that all the nonlinear scales are resolved. The legends are identical for all three figures.

cumulative dissipation $\sum_k \hat{\mathcal{D}}_{wk}$ given by

$$
\begin{aligned}
\widehat{\mathcal{D}}_{wk} =& \mathcal{R}\left[\widehat{\boldsymbol{w}}_{wk}^* \cdot \left(\frac{\mu}{\sqrt{\rho}\, Re_{ac}}\, \widehat{(\nabla \cdot (\nabla \boldsymbol{u} + \nabla \boldsymbol{u}^T))}\right)_{wk}\right] \\
&+ \mathcal{R}\left[\widehat{\left(p - \frac{1}{\gamma}\right)}_k^* \cdot \left(\frac{1}{Re_{ac}\, Pr}\, \widehat{\nabla \cdot (\alpha \nabla T')}\right)_k\right] \\
&+ \mathcal{R}\left[\widehat{\boldsymbol{w}}_{wk}^* \cdot \left(\frac{1}{\sqrt{\rho}\, Re_{ac}}\, \nabla \cdot \widehat{\left(\left(\kappa - \frac{2\mu}{3}\right)(\nabla \cdot \boldsymbol{u})\right)}\right)_k\right].
\end{aligned}
\tag{A1}
$$

As shown in figure 17(c), the values of scaled cumulative dissipation $\sum_k \widehat{\mathcal{D}}_{wk}/\varepsilon$ for $k_{max} = 1536$ overlap with those of $k_{max} = 1024$ for all the cases highlighting that the dissipation terms are converged. The $At = 0.5^\star$ case with $k_{max} = 768$ highlights how the spectral quantities look for an unresolved case, further highlighting that $k_{max} = 1024$ and $k_{max} = 1536$ results are converged.

Although the energy spectra deviate for $At = 0.75^\ddagger$ from $At = 0.75$ for $k\ell > 1024\ell$ slightly, the energy content in these scales is more than seven orders of magnitude smaller than integral length scales. Hence, these scales have a negligible contribution in dissipation. Consequently, $k_{max} = 1024$ is sufficient to resolve all the relevant dynamics in all the simulations discussed in this work.

Appendix B. Diffusion and dissipation time scale comparison

In this appendix, we compare the time scales across which Laplacian molecular diffusion and dissipation occur. To derive a time scale across which only molecular diffusion of active scalars driven by the Laplacian term occurs, we use the equation

$$
\frac{\partial Y_k}{\partial t} = \frac{D_1}{Re_{ac} Sc} \nabla^2 Y_k.
\tag{B1}
$$

Using scaling analysis, we obtain the time scale over which molecular diffusion (τ_m) of active scalars occurs as

$$
\frac{1}{\tau_m} \sim \frac{D_1}{Re_{ac} Sc L^2}.
\tag{B2}
$$

Combining (B2) and (3.16), we get the ratio of the molecular diffusion time scale (τ_m) to the nonlinear dissipation time scale (τ_d) as

$$
\frac{\tau_m}{\tau_d} \sim \frac{|D_2| Y_c}{D_1} \sim \frac{|1 - \chi| Y_c}{1 + (\chi - 1) Y_c}.
\tag{B3}
$$

Figure 18 shows the variation of the ratio of molecular diffusion time scale to nonlinear dissipation time scale with the concentration Y_c. The figure can be interpreted as the variation in time scales across the decaying moving interface. The concentration at the interface is high during the initial time, resulting in nonlinear dissipation occurring faster than molecular diffusion for $At < 0$. This results in the concentration gradient decaying less and mostly resulting in a shift/movement of the concentration gradients. But for the positive Atwood number, molecular diffusion occurs faster than nonlinear dissipation, resulting in more decay of gradients. For negative Atwood number cases, the nonlinear dissipation term dominates the molecular diffusion term, allowing higher gradients to
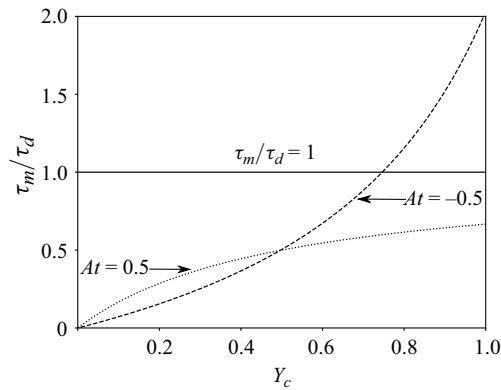
Figure 18. Variation of the ratio of Laplacian diffusion to dissipation time scales with concentration level of blob.

exist longer while for a positive Atwood number, molecular diffusion leads to the drop in $\langle |\nabla Y_c| \rangle$. This can also be inferred from the contours plots of $|\nabla Y_c|$ of figures 5(*a*) and 5(*b*).

REFERENCES

ABARZHI, S. 2002 A new type of the evolution of the bubble front in the Richtmyer–Meshkov instability. *Phys. Lett. A* **294** (2), 95–100.

AL-THEHABEY, O.Y. 2020 Modeling the amplitude growth of Richtmyer–Meshkov instability in shock–flame interactions. *Phys. Fluids* **32** (10), 104103.

ARNETT, D. 2000 The role of mixing in astrophysics. *Astrophys. J. Suppl.* **127** (2), 213–217.

ATKINSON, C., REUTER, G.E. & RIDLER-ROWE, C. 1981 Traveling wave solution for some nonlinear diffusion equations. *SIAM J. Math. Anal.* **12** (6), 880–892.

AUGIER, P., MOHANAN, A.V. & LINDBORG, E. 2019 Shallow water wave turbulence. *J. Fluid Mech.* **874**, 1169–1196.

BOYD, J. 2001 *Chebyshev and Fourier Spectral Methods*. Courier Corporation.

BROADWELL, J. & BREIDENTHAL, R. 1984 Structure and mixing of a transverse jet in incompressible flow. *J. Fluid Mech.* **148**, 405–412.

BROUILLETTE, M. 2002 The Richtmyer–Meshkov instability. *Annu. Rev. Fluid Mech.* **34** (1), 445–468.

BUCH, K.A. & DAHM, W.J. 1996 Experimental study of the fine-scale structure of conserved scalar mixing in turbulent shear flows. Part 1. *Sc* [Gt] 1. *J. Fluid Mech.* **317**, 21–71.

BURROWS, A. 2000 Supernova explosions in the Universe. *Nature* **403** (6771), 727–733.

CHO, H., VENTURI, D. & KARNIADAKIS, G. E. 2014 Statistical analysis and simulation of random shocks in stochastic burgers equation, *Proc. R. Soc. Lond. A: Math. Phys. Engng Sci.* **470** (2171), 20140080.

DIMOTAKIS, P.E. 2005 Turbulent mixing. *Annu. Rev. Fluid Mech.* **37** (1), 329–356.

DONZIS, D.A. 2012 Shock structure in shock-turbulence interactions. *Phys. Fluids* **24** (12), 126101.

ECKART, C. 1948 An analysis of the stirring and mixing processes in incompressible fluids. *J. Mar. Res.* **7**, 265–275.

ESWARAN, V. & POPE, S.B. 1988 An examination of forcing in direct numerical simulations of turbulence. *Comput. Fluids* **16** (3), 257–278.

GAO, F., ZHANG, Y., HE, Z. & TIAN, B. 2016 Formula for growth rate of mixing width applied to Richtmyer–Meshkov instability. *Phys. Fluids* **28** (11), 114101.

GAO, X., BERMEJO-MORENO, I. & LARSSON, J. 2020 Parametric numerical study of passive scalar mixing in shock turbulence interaction. *J. Fluid Mech.* **895**, A21.

GUPTA, P. & SCALO, C. 2018 Spectral energy cascade and decay in nonlinear acoustic waves. *Phys. Rev. E* **98** (3), 033117.

HERRMANN, M., MOIN, P. & ABARZHI, S.I. 2008 Nonlinear evolution of the Richtmyer–Meshkov instability. *J. Fluid Mech.* **612**, 311–338.

HIRSCHFELDER, J.O., CURTISS, C.F. & BIRD, R. 1964 *The Molecular Theory of Gases and Liquids*. John Wiley & Sons.

JOHN, J.P., DONZIS, D.A. & SREENIVASAN, K.R. 2019 Solenoidal scaling laws for compressible mixing. *Phys. Rev. Lett.* **123** (22), 224501.

JOSSY, J.P. & GUPTA, P. 2023 Baroclinic interaction of forced shock waves with random thermal gradients. *Phys. Fluids* **35** (5), 056114.

KUNDU, P.K., COHEN, I.M. & DOWLING, D. R. 2015 *Fluid Mechanics*. Academic press.

LARSSON, J., BERMEJO-MORENO, I. & LELE, S. K. 2013 Reynolds- and Mach-number effects in canonical shock–turbulence interaction. *J. Fluid Mech.* **717**, 293–321.

LI, H., TIAN, B., HE, Z. & ZHANG, Y. 2021 Growth mechanism of interfacial fluid-mixing width induced by successive nonlinear wave interactions. *Phys. Rev. E* **103** (5), 053109.

LIEPMANN, H. W. & ROSHKO, A. 2001 *Elements of Gasdynamics*. Courier Corporation.

LIU, H., YU, B., ZHANG, B. & XIANG, Y. 2022 On mixing enhancement by secondary baroclinic vorticity in a shock–bubble interaction. *J. Fluid Mech.* **931**, A17.

MESHKOV, E.E. 1969 Instability of the interface of two gases accelerated by a shock wave. *Fluid Dyn.* **4** (5), 101–104.

MEUNIER, P. & VILLERMAUX, E. 2003 How vortices mix. *J. Fluid Mech.* **476**, 213–222.

MIURA, H. & KIDA, S. 1995 Acoustic energy exchange in compressible turbulence. *Phys. Fluids* **7** (7), 1732–1742.

NI, Q. 2016 Compressible turbulent mixing: effects of compressibility. *Phys. Rev. E* **93** (4), 043116.

PANTANO, C., SARKAR, S. & WILLIAMS, F. 2003 Mixing of a conserved scalar in a turbulent reacting shear layer. *J. Fluid Mech.* **481**, 291–328.

POINSOT, T. & VEYNANTE, D. 2005 *Theoretical and Numerical Combustion*. RT Edwards, Inc.

RICHTMYER, R.D. 1954 Taylor instability in shock acceleration of compressible fluids. *Tech. Commun. Pure Appl. Maths* **13**, 297–319.

SAMTANEY, R., PULLIN, D.I. & KOSOVIĆ, B. 2001 Direct numerical simulation of decaying compressible turbulence and shocklet statistics. *Phys. Fluids* **13** (5), 1415–1430.

SARKAR, S. 1995 The stabilizing effect of compressibility in turbulent shear flow. *J. Fluid Mech.* **282**, 163–186.

SARKAR, S., ERLEBACHER, G., HUSSAINI, M. & KREISS, H.O. 1991 The analysis and modelling of dilatational terms in compressible turbulence. *J. Fluid Mech.* **227**, 473–493.

SCHUMACHER, J., SREENIVASAN, K.R. & YEUNG, P. 2005 Very fine structures in scalar mixing. *J. Fluid Mech.* **531**, 113–122.

SCHUMACHER, J. & SREENIVASAN, K.R. 2005 Statistics and geometry of passive scalars in turbulence. *Phys. Fluids* **17** (12), 125107.

SREENIVASAN, K.R. 2019 Turbulent mixing: a perspective. *Proc. Natl Acad. Sci. USA* **116** (37), 18175–18183.

TENNEKES, H. & LUMLEY, J.L. 1972 *A First Course in Turbulence*. MIT Press.

THOMAS, V.A. & KARES, R.J. 2012 Drive asymmetry and the origin of turbulence in an ICF implosion. *Phys. Rev. Lett.* **109** (7), 075004.

TIAN, Y., JABERI, F.A., LI, Z. & LIVESCU, D. 2017 Numerical study of variable density turbulence interaction with a normal shock wave. *J. Fluid Mech.* **829**, 551–588.

TOMKINS, C., KUMAR, S., ORLICZ, G. & PRESTRIDGE, K. 2008 An experimental investigation of mixing mechanisms in shock-accelerated flow. *J. Fluid Mech.* **611**, 131–150.

VILLERMAUX, E. 2019 Mixing versus stirring. *Annu. Rev. Fluid Mech.* **51** (1), 245–273.

WONG, M.L., BALTZER, J.R., LIVESCU, D. & LELE, S.K. 2022 Analysis of second moments and their budgets for Richtmyer–Meshkov instability and variable-density turbulence induced by reshock. *Phys. Rev. Fluids* **7** (4), 044602.

YANG, J., KUBOTA, T. & ZUKOSKI, E.E. 1993 Applications of shock-induced mixing to supersonic combustion. *AIAA J.* **31** (5), 854–862.

YU, B., LIU, H. & LIU, H. 2021 Scaling behavior of density gradient accelerated mixing rate in shock bubble interaction. *Phys. Rev. Fluids* **6** (6), 064502.

YUAN, M., ZHAO, Z., LIU, L., WANG, P., LIU, N.-S. & LU, X.-Y. 2023 Instability evolution of a shock-accelerated thin heavy fluid layer in cylindrical geometry. *J. Fluid Mech.* **969**, A6.

ZHANG, Q. 1998 Analytical solutions of layzer-type approach to unstable interfacial fluid mixing. *Phys. Rev. Lett.* **81** (16), 3391–3394.

ZHOU, Y. 2017 Rayleigh–Taylor and Richtmyer–Meshkov instability induced flow, turbulence, and mixing. II. *Phys. Rep.* **723**, 1–160.

ZHOU, Y., et al.et al. 2021 Rayleigh–Taylor and Richtmyer–Meshkov instabilities: a journey through scales. *Phys. D: Nonlinear Phenom.* **423**, 132838.

ZHOU, Y. 2024 *Hydrodynamic Instabilities and Turbulence: Rayleigh–Taylor, Richtmyer–Meshkov, and Kelvin–Helmholtz Mixing*. Cambridge University Press.

ZHOU, Y., SADLER, J. D. & HURRICANE, O. A. 2025 Instabilities and mixing in inertial confinement fusion. *Annu. Rev. Fluid Mech.* **57**.